Genetic determinants of *EGFR*-Driven Lung Cancer Growth and Therapeutic Response *In Vivo*

Giorgia Foggetti*[1], Chuan Li*[2], Hongchen Cai*[3], Jessica A. Hellyer[4], Wen-Yang Lin[3], Deborah Ayeni[1], Katherine Hastings[1], Jungmin Choi[5,6], Anna Wurtz[1], Laura Andrejka[3], Dylan Maghini[3], Nicholas Rashleigh[1], Stellar Levy[1], Robert Homer[7,8], Scott Gettinger[9], Maximilian Diehn[4,10,11], Heather A. Wakelee[4], Dmitri A. Petrov[2], Monte M. Winslow[3,12,13,#] and Katerina Politi[1,7,9,#]

[1]Yale Cancer Center, [5]Department of Genetics, [7]Pathology, [9]Medicine (Section of Medical Oncology), Yale School of Medicine, New Haven, Connecticut

[6]Department of Biomedical Sciences, Korea University College of Medicine, Seoul, Korea

[8]VA Connecticut HealthCare System, Pathology and Laboratory Medicine Service, West Haven, Connecticut

[2]Department of Biology, [3]Genetics, [4]Stanford Cancer Institute, Department of Medicine, Division of Oncology, [10]Institute for Stem Cell Biology and Regenerative Medicine, [11]Department of Radiation Oncology, [12]Pathology, [13]Cancer Biology Program, Stanford University School of Medicine, Stanford, California

* Authors contributed equally

To whom correspondence should be addressed:

Katerina Politi, PhD
Departments of Pathology and Internal Medicine (Section of Medical Oncology)
Yale Cancer Center
Yale University School of Medicine
333 Cedar Street, SHM-I 234D
New Haven, CT 06510 USA
Office Tel: 203-737-5921
Lab Tel: 203-737-6215
Fax: 203-785-7531
Email: katerina.politi@yale.edu

Monte Winslow, PhD
Departments of Genetics and Pathology
Stanford University School of Medicine
279 Campus Drive, B256
Stanford, CA 94305 USA
Office Tel: 650-725-8696
Email: mwinslow@stanford.edu

Abstract

Cancer genome sequencing has uncovered substantial complexity in the mutational landscape of tumors. Given this complexity, experimental approaches are necessary to establish the impact of combinations of genetic alterations on tumor biology and to uncover genotype-dependent effects on drug sensitivity. In lung adenocarcinoma, *EGFR* mutations co-occur with many putative tumor suppressor gene alterations, however the extent to which these alterations contribute to tumor growth and their response to therapy *in vivo* has not been explored experimentally. By integrating a novel mouse model of oncogenic *EGFR*-driven *Trp53*-deficient lung adenocarcinoma with multiplexed CRISPR–Cas9-mediated genome editing and tumor barcode sequencing, we quantified the effects of inactivation of ten putative tumor suppressor genes. Inactivation of *Apc*, *Rb1*, or *Rbm10* most strongly promoted tumor growth. Unexpectedly, inactivation of *Lkb1* or *Setd2* – which are the strongest drivers of tumor growth in an oncogenic *Kras*-driven model – reduced *EGFR*-driven tumor growth. These results are consistent with the relative frequency of these tumor suppressor gene alterations in human *EGFR*- and *KRAS*-driven lung adenocarcinomas. Furthermore, *Keap1* inactivation reduces the sensitivity of *EGFR*-driven *Trp53*-deficient tumors to the EGFR inhibitor osimertinib. Importantly, in human *EGFR/TP53* mutant lung adenocarcinomas, mutations in the KEAP1 pathway correlated with decreased time on tyrosine kinase inhibitor treatment. Our study highlights how genetic alterations can have dramatically different biological consequences depending on the oncogenic context and that the fitness landscape can shift upon drug treatment.

60 During tumor evolution, cancer cells accumulate alterations in oncogenes and tumor
61 suppressor genes, which contribute to many of the hallmarks of cancer[1]. Despite their extensive
62 genomic complexity, tumors are frequently classified based on the presence of a single
63 oncogenic driver mutation, while the function of co-incident tumor suppressor gene alterations
64 is largely ignored. There is emerging evidence that the interplay between oncogenic drivers and
65 tumor suppressor genes may influence tumor fitness and impact treatment response[2].
66 However, the combinatorially vast landscape of genomic alterations makes it difficult, except in
67 the most extreme cases, to glean information about the epistatic interactions between tumor
68 suppressor genes and oncogenes from human cancer sequencing data alone[3]. This complexity
69 makes inferring the relationship between genotype and therapy response even more tenuous.
70 Recently, high-throughput, tractable systems that combine autochthonous mouse modeling
71 and genome editing have been developed to directly uncover the functional consequences of
72 genetic alterations during tumorigenesis *in vivo*[4-10]. However, very few studies have
73 investigated the biological consequences of inactivating tumor suppressor genes in the context
74 of different oncogenic drivers *in vivo*, and existing knowledge about the role of specific genetic
75 alterations in tumor suppressor genes has been primarily inferred from correlative human
76 studies[11-13].
77 In lung adenocarcinoma, *EGFR* and *KRAS* are the two most frequently mutated oncogenic
78 driver genes and occur within a background of diverse putative tumor suppressor gene
79 alterations[2,11,12,14]. Among these, *TP53* is the most commonly mutated tumor suppressor gene
80 in both oncogenic *EGFR*- and *KRAS*-driven lung adenocarcinoma, consistent with the
81 importance of disrupting this pathway during lung cancer development[2,13,15-18]. Interestingly,
82 many other putative tumor suppressor genes are mutated at different frequencies in oncogenic
83 *EGFR*- and *KRAS*-driven lung adenocarcinomas[2,11,15]. Whether these differences are due to

84 different fitness effects that depend on the oncogenic context has never been tested
85 experimentally. Indeed, previous studies on tumor suppressor genes in lung cancer models *in*
86 *vivo* have been primarily conducted in the context of oncogenic *Kras*-driven tumors, while the
87 functional importance of different tumor suppressor genes in *EGFR*-driven lung tumors remains
88 largely unstudied (**Supplemental Fig. 1a**).
89 In addition to driving growth, inactivation of tumor suppressor pathways may affect the
90 therapeutic response to therapies. In advanced *EGFR* mutant lung adenocarcinomas, treatment
91 with EGFR tyrosine kinase inhibitors (TKIs) is the first-line of therapy[19-22]. Response rates to TKIs
92 are high, however, there is large variability in the depth and duration of response between
93 patients, and acquired resistance inevitably occurs[14]. Genomic alterations, including those in
94 *RB1* and *TP53*, have been found to correlate with clinical responses to TKIs[13,17,23]. However,
95 given the complexity and diversity of genomic alterations in these tumors, the functional
96 contribution of individual genes to drug resistance remains poorly understood.
97 To quantify the functional importance of a panel of ten diverse putative tumor suppressor
98 genes on oncogenic *EGFR*-driven lung tumor growth *in vivo,* we coupled multiplexed CRISPR–
99 Cas9-mediated somatic genome editing and tumor barcoding sequencing (Tuba-seq) with a
100 novel genetically engineered mouse model of $EGFR^{L858R}$-driven *Trp53*-deficient lung cancer.
101 Through the comparison of tumor suppressor effects in oncogenic *EGFR*- and *Kras*-driven lung
102 cancer models, we uncovered prevalent epistasis between the oncogenic drivers and tumor
103 suppressor genes, which explains the different mutational spectra of these tumor suppressor
104 genes in oncogenic *EGFR*- and *KRAS*-driven human lung adenocarcinomas. Moreover, we
105 established a direct causal link between tumor suppressor genotypes and differential responses
106 to osimertinib treatment in *EGFR*-driven lung adenocarcinoma that are supported by correlative
107 human mutational datasets.

108 **Results**

109 **Development of a lentiviral-Cre based mouse model of oncogenic *EGFR*-driven lung**

110 **adenocarcinoma**

111 The use of lentiviral vectors to initiate tumors in genetically engineered mouse models

112 of human cancer enables control of tumor multiplicity, tumor barcoding to map clonality, and

113 the delivery of lentivirus-encoded cDNAs, shRNAs, and sgRNAs to modify neoplastic cells[6,8,24,25].

114 The simplicity of viral-Cre initiated models of oncogenic *Kras*-driven lung cancer has enabled

115 the analysis of many genes that co-operate to drive tumor growth within these autochthonous

116 mouse models[26] (**Supplemental Fig. 1a**). To permit the generation of virally-initiated oncogenic

117 *EGFR*-driven *Trp53*-deficient lung tumors, we bred mice with an rtTA/tetracycline-inducible

118 transgene encoding the common lung adenocarcinoma-associated $EGFR^{L858R}$ mutant (*TetO-*

119 $EGFR^{L858R}$), a Cre-regulated *rtTA* transgene ($Rosa26^{CAGs\text{-}LSL\text{-}rtTA3\text{-}IRES\text{-}mKate}$, abbreviated $R26^{RIK}$), and

120 homozygous *Trp53* floxed alleles ($p53^{flox/flox}$)[27-29]. In these $TetO\text{-}EGFR^{L858R};Rosa26^{RIK};p53^{flox/flox}$

121 (*EGFR;p53*) mice, lentiviral-Cre transduction of lung epithelial cells leads to the expression of

122 rtTA and mKate as well as the inactivation of *Trp53*. Co-incident doxycycline treatment induces

123 the expression of oncogenic EGFR (**Fig. 1a**).

124 We initiated tumors with a lentiviral-PGK-Cre vector[30] in *EGFR;p53* mice and used

125 magnetic resonance imaging (MRI) to monitor tumor development (**Fig. 1b**). Tumors were first

126 detectable in *EGFR;p53* mice 8 weeks after tumor initiation. Histological analysis of lungs 11

127 weeks after tumor initiation confirmed the development of multifocal lung adenocarcinomas

128 (**Fig. 1b**, bottom panels). Tumors stained positively for $EGFR^{L858R}$ and mKate, as well as

129 surfactant protein C (SP-C) and the lung lineage-defining transcription factor NKX2.1/TTF-1 (**Fig.**

130 **1c**, top panels)[31-33]. Importantly, in this model, tumors were more focal than the diffuse tumors
131 that rapidly develop in the previous *CCSP-rtTA;TetO-EGFR*^{L858R} model[27] likely due to tumor
132 initiation from fewer cells in the virally initiated model (**Fig. 1b**, top right panel). Lentivirus-
133 induced tumors in *EGFR;p53* mice were more poorly differentiated than those typically
134 observed in the *CCSP-rtTA;TetO-EGFR*^{L858R} model (**Fig. 1b**, bottom panels) as shown by
135 increased prevalence of a micropapillary pattern, which is known to be highly aggressive in
136 human adenocarcinoma[27]. Thus, this new lentiviral-Cre-initiated model recapitulates the
137 genetic and histopathological features of human oncogenic *EGFR*-driven *TP53*-deficient lung
138 tumors.
139
140 **Multiplexed quantification of tumor suppressor gene function in *EGFR*-driven lung tumors**
141 To enable somatic genome editing in the *EGFR;p53* model, we further incorporated a
142 conditional *Cas9* allele (*Rosa26*$^{LSL\text{-}Cas9\text{-}GFP}$)[4] to generate *TetO-EGFR*^{L858R}*;R26*$^{RIK/LSL\text{-}Cas9\text{-}GFP}$*;p53*$^{flox/flox}$
143 (*EGFR;p53;Cas9*) mice (**Fig. 1a**). Lentiviral-Cre delivery to *EGFR;p53;Cas9* mice initiated
144 multifocal lung adenomas and adenocarcinomas that expressed EGFR^{L858R}, mKate, Cas9, and
145 GFP (**Figs. 1c, d**). Tumors in *EGFR;p53;Cas9* mice were histologically similar to those in the
146 *EGFR;p53* mice (**Figs. 1b, d** and **Supplemental Fig. 1b**).
147 We used an improved version of our Tuba-seq approach to quantify tumor suppressor
148 gene function in oncogenic *EGFR*-driven lung tumors (**Methods**). Genomic integration of
149 barcoded lentiviral vectors uniquely tags each transduced cell and all of the neoplastic cells
150 within the resulting clonal tumors[8]. Each barcode encodes an 8-nucleotide sgID region specific
151 to the sgRNA followed by a random 15-nucleotide barcode; thus, high-throughput sequencing

152 of this sgID-BC region from bulk tumor-bearing lung can be used to quantify the number of cells
153 in each tumor of each genotype (**Methods**)[8]. With this approach, the absolute number of
154 neoplastic cells in each tumor is calculated by normalizing the number of reads of each unique
155 barcode (sgID-BC) to the number of reads from benchmark control cells added to each sample
156 (**Fig. 2a**, **Supplemental Fig. 9a and Methods**). Thus, Tuba-Seq enables the parallel analysis of
157 the impact of multiple tumor suppressor gene alterations on tumor growth *in vivo.*
158 To assess the function of ten diverse putative tumor suppressor genes, which are
159 frequently altered in human lung adenocarcinoma, we initiated tumors in *EGFR;p53* and
160 *EGFR;p53;Cas9* mice with a pool of barcoded Lenti-sgRNA/*Cre* vectors (Lenti-sgTS^{Pool}/*Cre*; **Fig.**
161 **2a**). In addition to Lenti-sgRNA/*Cre* vectors targeting each putative tumor suppressor gene, this
162 pool contains negative control vectors, including four Lenti-sg*Inert/Cre* vectors and a vector
163 with an sgRNA targeting *Trp53* (which is already inactivated by Cre-mediated recombination in
164 *EGFR;p53;Cas9* mice, **Fig. 1a**)[8]. Lenti-sgTS^{Pool}/*Cre*-initiated tumors were first detectable by MRI 4
165 weeks after tumor initiation in *EGFR;p53;Cas9* mice. At 11 weeks after tumor initiation, when
166 tumors were readily detectable in all mice, tumor-bearing lungs were collected for Tuba-seq
167 analysis and histology (**Fig. 2b** and **Supplemental Fig. 1e**).
168
169 **Putative tumor suppressor genes have distinct effects on *EGFR*-driven lung tumor growth**
170 We used Tuba-seq to quantify the number of neoplastic cells in clonal tumors of each
171 genotype in the *EGFR;p53* model and used two summary statistics to describe the tumor size
172 distribution (percentiles within the tumor size distributions and the log-normal mean[34]
173 (**Methods**; **Figs. 2c-e** and **Supplemental Figs. 2a, b**)). Effects of the sgRNAs on tumor growth

174 were assessed by examining the significance of the differences in the tumor size distribution
175 compared to controls and also the magnitude of the effects. For negative controls, tumors with
176 each sgRNA in *EGFR;p53* mice, which lack the *Cas9* allele, had very similar size distributions (**Fig.**
177 **2d**). Furthermore, in *EGFR;p53;Cas9* mice, tumors initiated with each Lenti-sg*Inert/Cre* vector or
178 Lenti-sg*p53/Cre* had very similar tumor size profiles (**Figs. 2c, e**).

179 Inactivation of *Rb1*, *Apc*, and *Rbm10* most dramatically enhanced the growth of oncogenic
180 *EGFR*-driven *Trp53*-deficient lung tumors (**Figs. 2c, e**). While the importance of *RB1* inactivation
181 in *EGFR*-driven lung adenocarcinomas has begun to be investigated[23,35], very few studies have
182 addressed the functional importance of the APC pathway on *EGFR*-driven lung
183 adenocarcinomas[34]. Interestingly RBM10 is an RNA binding protein and splicing regulator that is
184 poorly studied in cancer in general and has not previously been implicated as a critical regulator
185 of *EGFR*-driven lung cancer growth[12,36-38].

186 Surprisingly, inactivation of either *Lkb1* or *Setd2* – which are strong tumor suppressor
187 genes in analogous oncogenic *Kras*-driven lung tumor models – dramatically reduced tumor
188 growth relative to sg*Inert* tumors[8,39,40]. These effects were consistent across multiple
189 percentiles within the tumor size distribution and as assessed by the LN mean of tumor sizes
190 (**Figs. 2c, e**). Notably, these significant effects observed with sg*Setd2*, sg*Lkb1*, sg*Smad4*, sg*Apc*,
191 sg*Rbm10*, and sg*Rb1* were all recaptured even after we simulated a 50% reduction in cutting
192 efficiency or when we used other strategies for subsampling underscoring the robustness of our
193 findings (**Supplemental Figs. 9b, c** and **Supplemental Figs. 10a, b**). These results suggest that in
194 specific contexts, inactivation of genes presumed to be tumor suppressors can have deleterious

195 effects on cancer growth. Other tumor suppressor genes, *Atm*, *Arid1a*, *Cdkn2a* and *Keap1*, did
196 not significantly alter tumor growth in the context of this experiment (**Figs. 2c, e**).
197 To assess tumor suppressor gene function at a later time point of tumor growth, we
198 initiated tumors in *EGFR;p53;Cas9* mice with 10-fold less Lenti-sgTS^{Pool}/*Cre* and performed
199 Tuba-seq after 19 weeks of tumor growth. At this time point, the histology of the tumors was
200 similar to that observed after 11 weeks of tumor initiation (**Supplemental Figs. 1c, d**). Tuba-seq
201 analysis confirmed the tumor-suppressive function of *Rbm10*, *Apc,* and *Rb1* (**Supplemental Figs.**
202 **2a-c**). Since we used a 10-fold lower viral titer for this experiment, there were proportionally
203 fewer tumors (**Supplemental Fig. 1f**), which limited the resolution of Tuba-seq analysis. Thus,
204 while inactivation of the other genes had no significant effect on tumor growth at this time
205 point, we cannot exclude that these genes may influence tumor growth. Interestingly, despite
206 the decreased statistical power, inactivation of *Cdkn2a* or *Arid1a* had a positive effect on tumor
207 growth at this 19-week time point (but not at the 11-week time point) suggesting a potential
208 role of these tumor suppressor genes during a later phase of tumorigenesis in this model
209 (**Supplemental Figs. 2a, b**).
210
211 **Validation of *Apc* and *Rbm10*-mediated tumor suppression**
212 We performed further experiments to confirm the role of two less-well studied tumor
213 suppressors, Apc and Rbm10 on the growth of *EGFR*-driven tumors. We initiated lung tumors in
214 *EGFR;p53* and *EGFR;p53;Cas9* mice with Lenti-sg*Apc*/*Cre*, Lenti-sg*Neo2*/*Cre* (sgInert), and two
215 Lenti-sg*Rbm10/Cre* vectors each with a unique sgRNA targeting *Rbm10* (*N* = 3 *EGFR;p53*
216 mice/group and *N* = 5 *EGFR;p53;Cas9* mice/group; **Fig. 3a**). We used two sgRNAs targeting

217 *Rbm10* to increase the power of our findings, and because the tumor suppressive role of *Rbm10*
218 remains entirely uncharacterized in *EGFR*-driven lung cancer. We found a large variation across
219 mice due to the stochastic nature of tumor progression and the low resolution of the tumor
220 volume measurements determined by MRI and through tumor area calculations (**Supplemental**
221 **Figs. 3b, c**). Despite this, inactivation of either *Apc* or *Rbm10* in *EGFR;p53;Cas9* mice gave rise to
222 tumors that were significantly larger than control tumors initiated with sg*Neo2* in
223 *EGFR;p53;Cas9* mice. Moreover, by quantifying the size of individual sg*Apc*- or sg*Rbm10*-
224 initiated tumors (based on tumor diameter) in histological sections, we observed that
225 *EGFR;p53;Cas9* tumors were larger than tumors initiated in *EGFR;p53* mice (**Figs. 3b-e**). Lenti-
226 sg*Apc*/Cre-initiated tumors in *EGFR;p53;Cas9* mice had more cancer cells with stabilization and
227 nuclear localization of β-catenin as well as increased expression of Sox9 (consistent with *Apc*
228 inactivation) (**Supplemental Figs. 3d, e**) [41]. Furthermore, at least 50% of Lenti-sg*Rbm10/Cre*-
229 initiated tumors in *EGFR;p53;Cas9* mice lacked or had lower Rbm10 protein (**Supplemental Fig.**
230 **3f**). Tumors with either *Apc* or *Rbm10* inactivation were histologically similar to tumors in
231 *EGFR;p53* mice at this time point and had papillary/acinar or micropapillary structures with a
232 medium/high nuclear grade (**Supplemental Fig. 3a**). These results further confirm the
233 importance of these tumor suppressor pathways in constraining *EGFR*-driven tumor growth *in*
234 *vivo.* Collectively, our findings underscore the value of coupling Tuba-seq and CRISPR–*Cas9*-
235 mediated somatic genome editing with our virally-induced mouse model to dissect gene
236 function in oncogenic *EGFR*-driven lung cancer.
237
238 **Oncogenic drivers shape the fitness landscape of tumor suppression**

239 The extent to which different oncogenic drivers affect the landscape of tumor
240 suppression is almost entirely unknown. We approached this question by comparing the fitness
241 landscape of tumor suppression within the contexts of oncogenic *EGFR*- and *Kras*-driven lung
242 tumors. We repeated an experiment previously performed by our group in which we
243 inactivated the same panel of tumor suppressor genes in *Kras*$^{LSL\text{-}G12D/+}$;*p53*$^{flox/flox}$;*R26*$^{LSL\text{-}}$
244 ^{Tomato};*H11*$^{LSL\text{-}Cas9}$ (*Kras;p53;Cas9*) mice and used library preparation methods and the analytical
245 pipeline identical to those used for the *EGFR;p53* and *EGFR;p53;Cas9* mice (**Supplemental Fig.**
246 **4a**)[29,30,42]. Inactivation of *Lkb1*, *Setd2,* and *Rb1* were particularly strong drivers of oncogenic
247 *Kras*-driven *Trp53*-deficient tumor growth, while inactivation of *Rbm10*, *Apc*, *Cdkn2a* and *Arid1a*
248 also modestly increased tumor growth (**Figs. 4a, b**). These results are largely consistent with our
249 previous Tuba-seq analysis of *Kras;p53;Cas9* mice, as well as other studies on these genes in
250 oncogenic *Kras*-driven lung cancer mouse models (**Supplemental Fig. 1a**)[9,39-41,43-47]
251 Inactivation of several of the tumor suppressor genes (e.g. *Rb1*) had similar effects on
252 *EGFR*- and *Kras*-driven tumors suggesting that these putative tumor suppressor genes limit lung
253 adenocarcinoma growth regardless of the oncogenic context in these mouse models (**Fig.4c** and
254 **Supplemental Fig. 4b**). However, inactivation of either *Lkb1* or *Setd2* greatly increased the
255 growth of oncogenic *Kras*-driven lung tumors but decreased the growth of oncogenic *EGFR*-
256 driven lung tumors (**Figs. 2c, e**, **Figs. 4a-c** and **Supplemental Fig. 4b**). Thus, the consequences of
257 tumor suppressor gene inactivation in specific contexts are not limited to the magnitude of
258 tumor-suppressive effects but can also be manifested as opposite effects (known as the sign
259 epistasis) even when the driving oncogenic alterations (in this case *EGFR* and *KRAS*) are
260 traditionally thought to be within a linear pathway.

261

262 **Profound epistasis between tumor suppressor genes and oncogenic drivers drives mutational**

263 **patterns in human lung adenocarcinoma**

264 To compare our functional data from our *in vivo* models with the spectrum of tumor

265 suppressor gene mutations found in human lung adenocarcinomas, we queried data from the

266 AACR Project GENIE database[48]. We calculated the frequency of tumor suppressor gene

267 mutations that occur co-incident with oncogenic *EGFR* (L858R, Exon 19 deletions, L861Q,

268 G719X) or oncogenic *KRAS* (at codons 12, 13 or 61) mutations and *TP53* mutations. This analysis

269 revealed different frequencies of mutations in several tumor suppressor genes in *EGFR/TP53*

270 and *KRAS/TP53* mutant human lung tumors. *RB1*, *RBM10*, and *APC* are frequently altered tumor

271 suppressor genes in *EGFR/TP53* mutant lung adenocarcinomas. Interestingly, *RB1* mutations are

272 more frequent in *EGFR/TP53* tumors compared to *KRAS/TP53* tumors (7.5% versus 3.1%).

273 However, *Rb1* inactivation was a major driver of tumor growth in both *EGFR* and *Kras* mutant

274 tumors in mice (**Figs. 2c, e** and **Figs. 4a-c**). This apparent discrepancy between mouse and

275 human may be related to the higher frequency of alterations in *CDKN2A* in human *KRAS/TP53*

276 mutant tumors (7.3%, **Fig. 4d**) that would disrupt the same cell cycle regulation pathway as *RB1*

277 inactivation. *LKB1/STK11* and *SETD2,* are among the most frequently mutated tumor

278 suppressor genes in *KRAS/TP53* mutant lung adenocarcinomas (**Fig. 4d**)[49,50]. Further supporting

279 a difference in the function of *LKB1* and *SETD2* in *EGFR/TP53* versus *KRAS/TP53* mutant lung

280 adenocarcinomas, mutations in these genes occurred at significantly higher frequencies in

281 *KRAS/TP53* mutant tumors compared to *EGFR/TP53* tumors (**Fig. 4e**). This asymmetry in the

282 mutation frequency of *LKB1* or *SETD2* within oncogenic *EGFR*- or *KRAS*-driven lung tumors is

283 also significant when we extend our analysis to include all tumors regardless of *TP53* mutation

284 status (**Supplemental Fig. 4c**). Collectively, the mouse and human data indicate that the

285 mutational patterns can reflect the biological consequences of profound epistasis between
286 tumor suppressor genes and oncogenic drivers. This highlights the power of our approach in
287 uncovering the functional relevance of genomic combinations on tumorigenesis.
288
289 ***Keap1* inactivation limits the response of tumors to osimertinib**
290 Genetically engineered mouse models have provided insight into the biology of *EGFR*-
291 driven lung tumors and proven valuable in studying mechanisms of resistance to EGFR TKIs,
292 especially on-target [51] mechanisms of resistance[27,52-54]. The TKI osimertinib was recently
293 approved for the first-line treatment of *EGFR*-driven lung adenocarcinomas. However,
294 pathways involved in modulating the depth of response and mechanisms of resistance to
295 osimertinib are still under investigation[55,56]. To investigate how tumor suppressor genes
296 influence the therapeutic response of lung tumors to EGFR inhibition, we treated
297 *EGFR;p53;Cas9* mice with Lenti-sgTS^{Pool}/*Cre*-initiated tumors with osimertinib for two weeks
298 starting at 9 weeks after tumor initiation (**Fig. 5a**). Osimertinib treatment greatly reduced the
299 overall tumor burden relative to vehicle-treated *EGFR;p53;Cas9* mice (**Supplemental Figs. 5a-d**).
300 Residual neoplastic cells were sparse, as determined by staining for $EGFR^{L858R}$ and those cells
301 were not proliferating (**Supplemental Figs. 5e-f**). The overall tumor response was similar when
302 the 2-week treatment was started 17 weeks after tumor initiation (**Supplemental Figs. 5g-j**).
303 To quantify the impact of inactivating each tumor suppressor gene on the response to
304 osimertinib *in vivo*, we performed Tuba-seq on the lungs from osimertinib-treated
305 *EGFR;p53;Cas9* mice 11 and 19 weeks after tumor initiation and compared the results to Tuba-
306 seq results from vehicle-treated controls (**Fig. 5b** and **Supplemental Figs. 6a, b**). Consistent with
307 the imaging data and histological analysis, osimertinib treatment greatly reduced tumor burden
308 as assessed by Tuba-seq (**Compare Figs 2c, e with Fig. 5b and Supplemental Fig. 6a**; **Methods**).

309 After two weeks of osimertinib treatment, inactivation of *Apc*, *Rb1* or *Rbm10* was still
310 associated with larger tumors while the size distribution of tumors with inactivation of *Cdkn2a*,
311 *Arid1a*, or *Atm* remained similar to that of tumors with inert sgRNAs (compare **Fig. 5b** and **Fig.**
312 **2e, Supplemental Fig. 6a** and **Fig. 2c**, **Supplemental Fig. 6b** and **Supplemental Fig. 2a**). The
313 striking exception was tumors with sg*Keap1*. In vehicle-treated mice, the size distribution of
314 sg*Keap1* tumors was almost identical to that of tumors with inert sgRNAs, however in
315 osimertinib-treated mice sg*Keap1* tumors were significantly larger than the tumors with inert
316 sgRNAs. This suggests that inactivation of *Keap1* limits responses to osimertinib (**Fig. 5b**).
317 Osimertinib resistance conferred by *Keap1* inactivation was also observed at 19 weeks after
318 tumor initiation (**Supplemental Figs. 6a, b**).
319 We applied an analytical approach that we previously developed and validated to
320 quantify the genotype-specific responses (**Fig. 5c** and **Supplemental Figs. 6c-g**; **Methods**)[57]. By
321 comparing the LN mean of the observed tumor size distributions in osimertinib-treated mice
322 with the expected tumor size distribution based on the overall drug effects, we can estimate
323 genotype specific drug responses (*ScoreRLM*; **Fig. 5c** and **Supplemental Fig. 6c**). At 11 weeks
324 after tumor initiation, following 2 weeks of osimertinib treatment sg*Rb1* tumors were 25%
325 smaller than expected (P = 0.04). Conversely, tumors with *Keap1* inactivation were 48% larger
326 than expected (P = 0.07; **Fig. 5c**). The effect of *Keap1* inactivation was even greater at 19 weeks
327 after tumor initiation, where tumors were 274% larger than expected (P = 0.13, **Supplemental**
328 **Fig. 6c**). Given the magnitude of the *ScoreRLM* for sg*Keap1* at both time points (*ScoreRLM* =
329 0.57 and 1.90 after two weeks of treatment at 11 and 19 weeks after tumor initiation,
330 respectively), we combined the two independent *P*-values and confirmed that *Keap1*
331 inactivation significantly reduced the therapeutic response to osimertinib (Fisher's method, *P*-
332 value = 0.05). Other statistical measures of genotype-specific responses, including relative

333 tumor number (*ScoreRTN*) and relative geometric mean (*ScoreRGM*) did not significantly differ
334 between the treated and untreated groups (**Supplemental Fig. 6d**; **Methods**). Our analytical
335 methods allow us to uncover when effects are more pronounced on larger tumors (*ScoreRTN*
336 and *ScoreRGM* have much lower sensitivity when the effects are greater on larger tumors;
337 **Supplemental Figs. 6e-g**; **Methods**). Thus, our data are consistent with the resistance conferred
338 by *Keap1* inactivation being more pronounced in larger tumors.
339
340 ***Keap1*-deficient tumors have reduced sensitivity to osimertinib which correlates with clinical**
341 **outcomes**
342 To further investigate these findings, we initiated tumors with Lenti-sg*Keap1/Cre* in
343 *EGFR;p53* and *EGFR;p53;Cas9* mice followed by treatment with osimertinib or vehicle (**Figs. 5d,**
344 **e**). Osimertinib-treatment reduced the size and number of tumors in *EGFR;p53* mice compared
345 to vehicle-treated *EGFR;p53* mice (**Fig 5d** and **Supplemental Figs. 7a, b**). Conversely, osimertinib
346 treatment of Lenti-sg*Keap1/Cre*-initiated tumors in *EGFR;p53;Cas9* mice did not decrease tumor
347 size or number compared to vehicle-treated *EGFR;p53;Cas9* mice (**Figs. 5d, e** and **Supplemental**
348 **Figs. 7a, b**). Consistent with the inefficiency of CRISPR–Cas9-mediated genome editing in
349 somatic cells, some tumors initiated with Lenti-sg*Keap1/Cre* in *EGFR;p53;Cas9* mice retained
350 expression of Keap1 protein (**Fig. 5e** top panels). However, the tumors that remained in
351 osimertinib-treated *EGFR;p53;Cas9* mice all had medium to low/negative expression of Keap1
352 (**Fig. 5e**). Together, these data indicate that while *Keap1* inactivation is not positively selected
353 for during oncogenic *EGFR*-driven tumor growth, osimertinib treatment selects for cancer cells
354 expressing low/negative levels of *Keap1*, thus reducing the therapeutic response to the drug.
355 To correlate our findings with clinical data, we analyzed the effects of KEAP1 pathway
356 alterations on patient outcomes to EGFR inhibition in *EGFR/TP53* mutant lung

357 adenocarcinomas. Oncogenic *EGFR*-driven tumors with KEAP1 pathway inactivation have been
358 suggested to be less responsive to TKIs, and we confirmed this association in *EGFR/TP53* tumors
359 (**Figs. 6a, b**)[58]. Mutations in the *KEAP1/NFE2L2/CUL3* pathway were associated with a
360 significantly shorter time on EGFR TKI therapy compared with matched patients with
361 *KEAP1/NFE2L2/CUL3* wildtype tumors (5.8 versus 14.3 months, $P = 0.01$; Log-rank test, **Fig. 6a**;
362 **Supplemental Table 1**). This remained significant even after adjustment for potential
363 confounders such as age, sex, race and smoking status (**Supplemental Table 2**). Among several
364 other tumor suppressor genotypes, KEAP1 pathway alterations were the most significant driver
365 of limited sensitivity after correction for multiple hypothesis testing (**Fig. 6b**).
366 We also analyzed a dataset of oncogenic *EGFR* lung adenocarcinoma patient samples
367 collected through the Yale Lung Rebiopsy Program (YLR) prior to first-line TKI treatment
368 (erlotinib, gefitinib, or afatinib) and after the development of resistance to TKIs (**Fig. 6c**;
369 **Supplemental Table 3**). Among 18 patients with *EGFR* and *TP53* mutant tumors, two had *KEAP1*
370 alterations at relapse (TKI-R samples). One case had an acquired missense mutation (Y206N)
371 that lies in a domain of KEAP1 involved in forming the complex with Cullin3 to mediate
372 ubiquitination and degradation of NRF2 (encoded by *NFE2L2*)[59]. The other tumor, which was
373 analyzed only at resistance had heterozygous loss of *KEAP1* (**Fig. 6c**). Moreover, we also
374 observed two cases of *NFE2L2* copy number gain (one detected prior to treatment and
375 maintained at resistance, the other detected only at resistance), and one case of *CUL3*
376 heterozygous loss at resistance. Thus, our *in vivo* functional results are consistent with human
377 data and support a role for inactivation of the KEAP1 pathway in reducing EGFR TKI sensitivity.
378
379 **Discussion**

380 The genomic fitness landscape of lung adenocarcinoma is combinatorially complex, with
381 a large number of genomic alterations in oncogenic drivers and tumor suppressor genes
382 occurring in various combinations[2,3]. While critical for precision medicine approaches,
383 dissecting the functional contribution of these co-occurring genetic alterations to tumor growth
384 and response to therapy is extremely challenging. Using somatic CRISPR–Cas9-mediated gene
385 editing and Tuba-seq[8,9], we evaluated the fitness effects of inactivation of ten tumor suppressor
386 genes commonly altered in lung adenocarcinoma in the contexts of oncogenic *EGFR*- and *Kras*-
387 driven tumors. We uncovered distinct roles for specific tumor suppressor genes on tumor
388 growth in the different oncogenic contexts and on sensitivity to the TKI osimertinib *in vivo*.
389 *EGFR* and *KRAS* are the most frequently mutated oncogenic drivers in lung
390 adenocarcinoma, collectively occurring in ~40-50% of all patients[2]. Oncogenic alterations in
391 these two genes are mutually exclusive, consistent with them being in the same canonical
392 receptor tyrosine kinase (EGFR-RAS-MAPK) signaling pathway[60,61]. For this reason, one might
393 anticipate that inactivating tumor suppressor pathways in *EGFR*-driven and *KRAS*-driven lung
394 cancers would have similar biological consequences. It is tempting to make a simplifying
395 assumption that tumor suppressor genes have a constant marginal effect independent of other
396 genomic alterations, or in other words, that the fitness landscape of tumor suppression is
397 smooth and that epistatic interactions are infrequent and/or small in magnitude. Here, we
398 tested this assumption by comparing the fitness landscape of tumor suppression in *EGFR*-driven
399 *Trp53*-deficient and in *Kras*-driven *Trp53*-deficient lung adenocarcinoma and found pervasive
400 epistasis between tumor suppressor genes and oncogenes. Inactivation of *Rb1*, *Rbm10* and *Apc*
401 had a similar effect on *EGFR* and *KRAS*-driven lung tumors (**Figs. 2c, e**, **Figs. 4a-c** and
402 **Supplemental Figs. 4b**). However, while *Lkb1* and *Setd2* were amongst the most potent tumor
403 suppressor genes in *Kras/p53* tumors, sg*Lkb1* and sg*Setd2* led to reduced tumor growth of

404 *EGFR/p53* tumors (**Figs. 2c, e** and **Figs. 4a, b**). This observation is consistent with human data,
405 where alterations in either *LKB1* or *SETD2*, are much less common in lung tumors with
406 oncogenic *EGFR* than in tumors with oncogenic *KRAS* (**Figs. 4d, e** and **Supplemental Fig. 4c**).
407 Thus, we reveal a highly context-dependent fitness landscape of tumor suppression that
408 depends on the nature of the oncogenic driver. Investigation of the mechanisms that underlie
409 the sign epistasis of *LKB1* and *SETD2* may uncover new biological insights and vulnerabilities of
410 *EGFR* mutant tumors. More broadly, sign epistasis within seemingly similar cancer contexts,
411 could help identify genetic interactions for further functional investigation and should be
412 considered when interpreting cancer genomic data (**Figs. 4d, e** and **Supplemental Fig. 4c**).
413 One major advantage of autochthonous genetically engineered mouse models of human
414 cancer is that they can be used to study the impact of inactivation of putative tumor suppressor
415 genes on therapy responses *in vivo*[10,57,62]. We found that inactivation of *Keap1* decreases
416 sensitivity to osimertinib *in vivo* (**Fig. 5**). This finding was supported in a clinical cohort of
417 *EGFR/TP53* mutated lung adenocarcinomas, in which patients with tumors harboring mutations
418 in *KEAP1/NFE2L2/CUL*3 had a significantly shorter time to treatment discontinuation with EGFR
419 TKIs compared with matched controls (**Figs. 6a, b** and **Supplemental Figs. 8a-d**)[17,58]. These
420 results are consistent with this tumor suppressor gene pathway limiting the response to
421 therapy and explains the presence of alterations in *KEAP1* pathway genes in TKI-resistant
422 human tumors. A reduced response to TKI therapy mediated by *KEAP1* inactivation may be
423 associated with the accumulation and transactivation of oxidative stress-related genes by
424 NRF2[63-65]. Indeed, we found that Keap1-deficient tumors had increased nuclear Nrf2 and Nqo1
425 expression relative to Keap1-proficient tumors, suggesting enhanced Nrf2 transcriptional
426 activity (**Supplemental Fig. 7c**)[63-65]. Alternatively, KEAP1/NRF2-dependent metabolic
427 reprogramming could be involved in mediating drug resistance in lung cancer[66-68]. However,

428 direct genetic alterations in this pathway occur in less than 10% of TKI-resistant *EGFR* mutant
429 lung adenocarcinomas (**Fig. 6c**)[17]. It is possible that non-genomic alterations that increase
430 NRF2-dependent gene expression or other mechanisms that decrease oxidative stress also
431 occur in TKI-resistant tumors[69-72]. Collectively, these results raise the possibility that targeting
432 NRF2 may reduce or delay the onset of resistance in *EGFR*-driven lung adenocarcinomas. More
433 broadly, our study demonstrates that our approach can be used to identify clinically relevant
434 pathways that modulate response to therapy *in vivo*. By uncovering the driving forces of the
435 heterogeneity of responses to therapy observed in patients, these types of studies could help
436 define high-risk versus low-risk patient populations and guide therapeutic interventions.
437 This study provides insight into the complex interplay between tumor suppressor genes
438 and other co-occurring mutations in *EGFR*-driven lung adenocarcinoma tumorigenesis and thus
439 has significant clinical implications. By evaluating interactions between co-occurring alterations
440 in these models, we have avoided confounding factors pervasive in human genomic data (*i.e.,*
441 tumor mutation load, mutation frequency, passenger mutations) and environmental factors
442 such as smoking, a condition that is more often, but not exclusively associated with *KRAS*-driven
443 tumors. Our data provide clear quantitative data on mutual exclusivity and synergistic biological
444 effects of genetic alterations. Notably, other oncogenic drivers (e.g. an *ALK* rearrangement) also
445 have a unique spectrum of co-occurring tumor suppressor gene alterations further suggesting
446 wide-spread interactions between tumor suppressor gene pathways and oncogenic drivers
447 (**Supplemental Fig. 11**). Future *in vivo* Tuba-seq studies should investigate tumor models driven
448 by other oncogenes to uncover a broader understanding of the genetic interactions between
449 diverse oncogenes and large panels of tumor suppressor genes. Precise mapping of the fitness
450 consequences of combinations of genetic alterations during tumor evolution will help uncover
451 the biological and clinical relevance of specific alterations during carcinogenesis and identify

452 pathways that can be exploited as therapeutic targets to prevent or overcome resistance to
453 TKIs.
454
455 **Acknowledgements**
456 G.F was supported by an American Italian Cancer Foundation (AICF) postdoctoral
457 fellowship. C.L. is the Connie and Bob Lurie Fellow of the Damon Runyon Cancer Research
458 Foundation (DRG-2331). H.C. was supported by a Tobacco-Related Disease Research Program
459 Postdoctoral Fellowship (28FT-0019). D.A. was supported by NIH F31 CA203488. K.H. was
460 supported by NIH F32 CA210516. This work was supported by NIH R01 CA231253 (to M.M.W
461 and D.P), NIH R01 CA234349 (to M.M.W and D.P.), NIH R01 CA120247 (to K.P.) and NIH P50
462 CA196530 (to K.P.). The authors would like to acknowledge the American Association for Cancer
463 Research and its financial and material support in the development of the AACR Project GENIE
464 registry, as well as members of the consortium for their commitment to data sharing.
465 Interpretations are the responsibility of study authors. We thank members of the Politi,
466 Winslow and Petrov Laboratories for helpful feedback and support in particular, Jacqueline
467 Starrett and Emily Forrest for editing, Fernando de Miguel for creating resources to help with
468 the WES analysis. We also thank Henning Stehr for providing the sequencing data from the
469 STAMP cohort and the Bosenberg Laboratory for sharing their Leica M205 FA
470 stereomicroscope.
471
472 **Author contributions**
473 G.F. designed and performed *in vivo* experiments, analyzed the data and wrote the
474 manuscript. C.L. performed sequencing analysis, developed and performed statistical analyses,
475 and wrote the manuscript. H.C. designed sgRNAs, generated Lenti-sgRNA/*Cre* vectors, tested

476 sgRNA cutting efficiency, produced lentivirus, and wrote the manuscript. J.A.H. evaluated and
477 analyzed the Stanford Solid Tumor Actionable Mutation Panel (STAMP) cohort of lung cancer
478 patients at Stanford University School of Medicine and wrote the manuscript. W.L. performed
479 *in vivo* experiments, D.A. and K.H. developed the models used for the study. J.C. generated the
480 pipeline for the WES data of the Yale Rebiopsy program (YLR) cohort at the Yale Cancer Center.
481 A.W. coordinates the YLR program. L.A. prepared the libraries for Tuba-seq. D.M. developed the
482 pipeline to analyze the GENIE data. N.R. and S.L. maintained the Yale mouse colony and imaged
483 mice included in this study. R.H. performed the histological analysis of all the mouse lung tumor
484 samples. S.G. conceptualized and leads the Yale Rebiopsy Program at the Yale Cancer Center
485 with K.P.. M.D. conceptualized and analyzed the STAMP cases. H.W. supervised the analysis of
486 the STAMP cohort. D.A.P. conceptualized, supervised the project and wrote the manuscript.
487 M.M.W. and K.P. designed the experiments, conceptualized, supervised the project and wrote
488 the manuscript. All the authors have revised and approved the submitted version.
489

490 **Methods**

491 **Mice and tumor initiation**

492 *TetO-EGFR*^{L858R}; *p53*$^{flox/flox}$; *Rosa26*$^{CAGs\text{-}LSL\text{-}rtTA3\text{-}IRES\text{-}mKate}$, *Rosa26*$^{CAGs\text{-}LSL\text{-}Cas9\text{-}GFP}$, *Kras*$^{LSL\text{-}G12D}$,
493 *Rosa26*$^{LSL\text{-}tdTomato}$, and *H11*$^{LSL\text{-}Cas9}$ mice have been described[4,25,27-30,42,73,74]. *EGFR*;*p53* and
494 *EGFR*;*p53;Cas9* were on a mixed BL6/129/FVB background and *Kras*;*p53;Cas9* mice were on a
495 mixed BL6/129 background. Approximately equal numbers of males and females were used for
496 each experiment and the number of mice used for each experiment is listed in each figure
497 legend. Lung tumors were initiated by intratracheal administration of Lentiviral-*Cre* vectors as
498 previously described[26]. Tumor burden was assessed by magnetic resonance imaging,

499 fluorescence microscopy, lung weight, and histology, as indicated. Doxycycline was
500 administered by feeding mice with doxycycline-impregnated food pellets (625 ppm; Harlan-
501 Teklad). Osimertinib (from AstraZeneca, Cambridge, UK) was resuspended in 0.5% (w/v)
502 methylcellulose (vehicle) and was administered orally (*per os*, 25 mg/kg 5 days a week). All
503 animals were kept in pathogen-free housing under guidelines approved by either the Yale
504 University Institutional Animal Care or the Stanford University Institutional Animal Care and Use
505 Committee guidelines.
506

507 **Production, purification, and titering of lentivirus**

508 The barcoded vectors in the Lenti-sg*TS*^{Pool}*/Cre* have been previously described
509 (**Supplemental Table 4**)[8]. The second Lenti-sg*Rbm10/Cre* vector used in the validation
510 experiments was generated by site-directed mutagenesis (**Supplemental Table 5**). Briefly,
511 Lentiviral-U6-sgRNA*/Cre* vectors contain an 8-nucleotide defined sequence (sgID) that identifies
512 the sgRNA followed by a 15-nucleotide random barcode (BC) to uniquely tag each tumor[8]. To
513 avoid barcode-sgRNA uncoupling driven by lentiviral template switching during reverse
514 transcription of the pseudo-diploid viral genome, each barcoded Lenti-sgRNA*/Cre* vector was
515 generated separately[75,76]. We cultured HEK293T cells in Dulbecco's Modified Eagle Medium
516 with 10% Fetal Bovine Serum and transfected them with individual barcoded Lenti-sgRNA*/Cre*
517 plasmids (*sgLkb1, sgp53, sgApc, sgAtm, sgArid1a, sgCdkn2a, sgKeap1, sgNeo1, sgNeo2, sgNeo3,*
518 *sgNT1, sgRb1, sgRbm10, sgRbm10#2* unbarcoded*, sgSetd2,* or *sgSmad4*) along with pCMV-VSV-
519 G (Addgene #8454) envelope plasmid and pCMV-dR8.2 dvpr (Addgene #8455) packaging
520 plasmid using polyethylenimine. We treated the cells with 20 mM sodium butyrate 8 hours
521 after transfection, changed the culture medium 24 hours after transfection, and collected

522 supernatants 36 and 48 hours after transfection. Subsequently, we removed the cell debris with
523 a 0.45 µm syringe filter unit (Millipore SLHP033RB), concentrated each lentiviral vector by
524 ultracentrifugation (25,000 g for 1.5 hours at 4°C), resuspended the virus in PBS, and stored the
525 virus at -80°C. To determine the titer of each vector, we transduced *Rosa26*$^{LSL\text{-}YFP}$ mouse
526 embryonic fibroblasts (a gift from Dr. Alejandro Sweet-Cordero/UCSF), determined the
527 percentage of YFP-positive cells by flow cytometry, and normalized the titer to a lentiviral
528 preparation of known titer. Lentiviral vectors were thawed and pooled immediately prior to
529 delivery to mice. All these plasmids are available at
530 https://www.addgene.org/Monte_Winslow/.
531

532 **Lentiviral titers and time of analysis**

533 Anticipated growth rates were determined by monitoring tumor development through
534 magnetic resonance imaging in pilot experiments and the analysis time points were selected to
535 ensure that tumors were detectable by MRI such that their response to treatment could be
536 evaluated. Viral titers used in the experiments were chosen to balance the total tumor burden
537 across mice at the time of analysis after tumor initiation. For analysis of tumor growth 11 weeks
538 after tumor initiation, the Lenti-sg*TS*^{Pool}*/Cre* titer administered to *EGFR*;*p53* mice was 2x10^{6}
539 infectious units (ifu)/mouse, while for *EGFR*;*p53;Cas9* mice we used 1x10^{6} ifu/mouse. We
540 reasoned that using a higher viral titer in the control *EGFR;p53* mice would increase our
541 confidence that any differences observed between *EGFR;p53* and *EGFR;p53;Cas9* mice were
542 due to inactivation of tumor suppressor genes in the latter model. For the 19-week time point
543 in *EGFR*;*p53;Cas9* mice we initiated tumors with 1x10^{5} ifu/mouse. Two weeks before collection,
544 mice were treated with either vehicle or osimertinib. For the validation experiments in which
545 we used a single vector to initiate tumors (Lenti-sg*Apc/Cre*, Lenti-sg*Rbm10/Cre,* Lenti-

546 sg*Rbm10*#2*/Cre* or Lenti-sg*Neo2/Cre* (sg*Inert*)) we used 1x10^5 ifu/mouse and analyzed the mice
547 after 14 weeks of tumor growth (**Supplemental Table 5**). For the validation with Lenti-
548 sg*Keap1/Cre* virus (1x10^5 ifu/mouse), both *EGFR;p53* and *EGFR;p53;Cas9* mice were treated 15
549 weeks after tumor initiation and lungs were collected after two weeks of treatment with either
550 vehicle or osimertinib. *Kras*;*p53;Cas9* were analyzed 14 weeks after tumor initiation with
551 2.2x10^4 ifu/mouse.
552
553 **Magnetic resonance imaging**
554 All procedures were performed in accordance with protocols approved by the Yale
555 University IACUC and in agreement with the NIH Guide for the Care and Use of Laboratory
556 Animals. Respiratory gated, gradient-echo MR images of mice were collected with a 4T (31-cm
557 bore) small-animal Bruker horizontal-bore spectrometer (Bruker AVANCE). All data were
558 collected as previously described[52]. Tumor volume was quantified by calculating the area of
559 visible lung opacities present in each image sequence per mouse using BioImage Suite 3.01[77].
560
561 **Isolation of genomic DNA from mouse lungs and preparation of sgID-BC libraries**
562 Genomic DNA was isolated from bulk tumor-bearing lung tissue from each mouse as
563 previously described[8]. Briefly, three benchmark control cell lines (~5x10^5 cells per cell line)
564 carrying unique sgID-BCs, were added ("spiked-in") to each sample prior to lysis to enable the
565 calculation of the absolute number of neoplastic cells in each tumor from the number of sgID-
566 BC reads. Following homogenization and overnight protease K digestion, genomic DNA was
567 extracted from the lung lysates using standard phenol-chloroform and ethanol precipitation.

568 sgID-BC sequencing libraries were prepared by PCR amplifying the sgID-BC region from
569 total genomic DNA. To enable the identification and subsequent computational elimination of
570 index hopped reads after high-throughput sequencing, the sgID-BC region of the integrated
571 Lenti-sg*RNA-BC/Cre* vectors was PCR amplified using unique dual indexing primer pairs. To
572 increase the sequence diversity at each position and reduce the amount of PhiX required to
573 achieve high sequencing quality, we added 6-9 Ns before the sequence-specific primers[57]. PhiX
574 is control DNA (with a diverse sequence) that is added to Illumina sequencing samples when
575 the diversity of the product to be sequenced is low (often the case with amplicon sequencing
576 like what we are doing to analyze barcodes). Since we are performing amplicon sequencing
577 with the possibility of less than random sequence diversity at each position, we add 5%-15%
578 PhiX to ensure good sequencing quality. We used a single-step PCR amplification of sgID-BC
579 regions, which we have found to be a highly reproducible and quantitative method to
580 determine the number of neoplastic cells in each tumor. For each mouse, we performed eight
581 100 µl PCR reactions per sample (4 µg DNA per reaction, 32 µg per mouse) using Q5 High-
582 Fidelity 2x Master Mix (New England Biolabs, M0494X). The PCR products were purified with
583 Agencourt AMPure XP beads (Beckman Coulter, A63881) using a double size selection protocol.
584 The concentration and quality of the purified libraries were determined using the Agilent High
585 Sensitivity DNA kit (Agilent Technologies, 5067-4626) on the Agilent 2100 Bioanalyzer (Agilent
586 Technologies, G2939BA). The libraries were pooled based on lung weight (to have sequencing
587 depth more evenly distributed across samples), cleaned up and size-selected using AMPure XP
588 beads, and sequenced on the Illumina®HiSeq 2500 platform to generate paired-end 150 bp
589 reads (Admera Health).
590
591 **Quantification of tumor sizes from sgID-BC sequencing data**

592 A diagram describing the analysis steps that are part of the Tuba-seq method in more
593 detail are summarized in **Supplemental Fig. 9a**. We used stringent filtering to identify the sgID-
594 BC region that minimizes PCR and sequencing error, as previously described[57]. Specifically, we
595 required no mismatch in the barcode region between the forward and reverse reads and
596 removed all spurious tumors with the barcodes within two nucleotides from that of another
597 larger tumor. The absolute number of cells in each tumor was calculated by scaling its sgID-BC
598 read number with the mean read number of three spiked-in cell lines with a known absolute
599 cell number of $5x10^5$.
600
601 **Summary statistics for tumor size distributions**
602 As sequencing depth and PCR efficiency vary across libraries, we focused on tumors that
603 we can repeatedly identify with high confidence, which are tumors over 500 cells as quantified
604 by comparing technical replicates. We used multiple summary statistics to describe the
605 truncated distribution of tumor sizes for all tumors larger than 500 cells. Percentiles and LN
606 means were calculated as two summary statistics. Percentiles are a nonparametric summary of
607 the distribution by taking the 50th, 60th, 70th, 70th, 90th, and 95th percentile of the distribution.
608 The LN mean calculates the maximum likelihood estimator of the mean tumor sizes assuming a
609 log-normal distribution of tumor sizes. For both of these metrics, we normalized to the
610 corresponding value of the average of inert tumors to represent the relative growth advantage
611 of inactivating the gene.
612
613 **Quantification of treatment responses of inert tumors to osimertinib**
614 We quantified the treatment effect of osimertinib by comparing the tumor size
615 distributions of the vehicle- and osimertinib-treated groups. We used two ways to quantify

616 treatment effect. The first way is to calculate the total number of neoplastic cells of tumors
617 carrying the inert control sgRNAs in each mouse and taking the fold change of the average of
618 the total number of neoplastic cells as an approximation of the drug effect.

619 $$Drug\ effect = \frac{Average\ neoplastic\ cell\ number\ in\ osimertinib - treated\ mice}{Average\ neoplastic\ cell\ number\ in\ vehicle - treated\ mice}$$

620 This calculation of tumor burden is very intuitive and relevant in the clinical setting, but this
621 measure is quite variable due to the large variations in the sizes of the largest tumors. The
622 second way assumes that each neoplastic cell, regardless of the size of the tumor harboring it,
623 has an equal probability of being killed by osimertinib treatment (*K*). To make sure that we are
624 evaluating tumors that are large enough to be repeatedly identified, we focus on tumors that
625 are over 1,000 cells in the vehicle-treated mice. We estimated the tumor size reduction after
626 treatment with osimertinib for the tumors with the inert control sgRNAs by matching the
627 distribution of tumor sizes in vehicle- and osimertinib-treated mice. Specifically, we used the
628 binary search algorithm to find the proportion of neoplastic cells remaining after treatment
629 with osimertinib (*S*) between *K* = 1 (100% cells were killed by osimertinib) and *K* = 0 (0% of cells
630 were killed by osimertinib), such that the median tumor number of tumors with the inert
631 control sgRNAs across the vehicle-treated mice, upon simulated reduction to *K*, matches the
632 median tumor number of tumors with the inert control sgRNAs larger than 1,000 cells across all
633 osimertinib-treated mice.
634

635 **Estimation of genotype-specific treatment responses**

636 We calculated the expected size distribution of tumors after treatment assuming no
637 genotype-specific treatment responses by reducing all tumors in the vehicle-treated mice by
638 the estimated drug effect (*K*). Then we calculated the genotype-specific treatment response for

639 each sg*TS* by comparing the relative LN mean of all tumors in the osimertinib-treated mice and
640 the relative LN mean of all tumors calculated from the expected distribution after treatment.
641 The genotype-specific treatment response is calculated as the log2 ratio of the observed
642 relative LN mean by the expected LN mean, and we named it as *ScoreRLM*. We focus on tumors
643 with the inert control sgRNAs that are over 1,000 cells in untreated mice and take out
644 comparable proportions of tumors with each sgRNA from each vehicle- and osimertinib-treated
645 mice based on the estimated treatment effect and the proportion of tumors carrying each sg*TS*.
646 The *ScoreRLM* is calculated as:

647 $$RLM_{i,j} = Log_2\left(\frac{\text{LN mean}_{\text{i,osimertinib}} / \text{LN mean}_{\text{Inert,osimertinib}}}{\text{LN mean}_{\text{i,vehicle}} / \text{LN mean}_{\text{Inert,vehicle}}}\right)$$

648 $$ScoreRLM_{i,j} = 2^{RLM_{i,j}} - 1$$

649 where $\text{LN mean}_{\text{i,osimertinib}}$ is the LN mean for tumors containing sgID *i* in osimertinib-treated
650 group, $\text{LN mean}_{\text{Inert,osimertinib}}$ is the LN mean for all tumors containing one of the four inert
651 sgIDs in the osimertinib-treated group. Similarly, $\text{LN mean}_{\text{i,vehicle}}$ is the LN mean for tumors
652 containing sgID *i* in vehicle-treated group and $\text{LN mean}_{\text{Inert,vehicle}}$ is the LN mean for all tumors
653 containing one of the four inert sgIDs in the vehicle-treated group. When tumors are larger
654 than expected, the *ScoreRLM* will be positive, indicating resistance conferred by gene
655 inactivation, while when tumors are smaller than expected, the *ScoreRLM* will be negative,
656 indicating sensitivity conferred by tumor suppressor gene inactivation. Although the metric on
657 the log2 scale results in the first formula with good statistical properties ranging from $-\infty$ to +
658 ∞ and centered on 0. To make it more directly interpretable by readers, we converted it to the
659 linear scale as shown in the second formula. On the linear scale the metric ranges from -1 to +

660 ∞, a value of 0.5 means the tumors are 50% larger than expected and a value of -0.5 means

661 that the tumors are 50% smaller than expected.

662 Apart from *ScoreRLM* that compares the relative LN mean in the vehicle- and

663 osimertinib-treated group, we can similarly compare the relative tumor number (*ScoreRTN*) and

664 relative geometric mean (*ScoreRGM*) for the observed and expected distribution of tumor sizes

665 following the same logic as shown below:

666 $$ScoreRGM_{i,j} = Log_2\left(\frac{\text{geometric mean}_{\text{i,osimertinib}} / \text{geometric mean}_{\text{Inert,osimertinib}}}{\text{geometric mean}_{\text{i,vehicle}} / \text{geometric mean}_{\text{Inert,vehicle}}}\right)$$

667 $$ScoreRGM_{i,j} = 2^{RGM_{i,j}} - 1$$

668

669 $$RTN_{i,j} = Log_2\left(\frac{\text{tumor number}_{\text{i,osimertinib}} / \text{tumor number}_{\text{Inert,osimertinib}}}{\text{tumor number}_{\text{i,vehicle}} / \text{tumor number}_{\text{Inert,vehicle}}}\right)$$

670 $$ScoreRTN_{i,j} = 2^{RTN_{i,j}} - 1$$

671 where the geometric mean and tumor number were calculated from inert tumors that are over

672 1,000 cells in the vehicle-treated mice and the corresponding proportions for other sgIDs in the

673 vehicle-and osimertinib-treated groups considering the proportion of sgIDs and the

674 treatment[57].

675 The standard deviation of the genotype-specific responses, represented by any of the

676 three metrics, is estimated by bootstrapping mice in both the vehicle- and osimertinib-treated

677 groups and then bootstrapping tumors with the same sgID in each bootstrapped mouse. Such a

678 two-step bootstrap process allows us to control for both variations of tumor size across mice

679 and within the same mouse. For each run of bootstrap, we re-estimated the drug effect,

680 estimated the expected tumor size profile between the vehicle- and osimertinib-treated mice.

681 We estimated the standard deviation based on the scores on the log2 scale and then plotted
682 the values on the linear scale, because the latter ranges from -1 to +∞ with no genotype-
683 specific responses located at 1.
684
685 **Power analysis for three metrics in identifying genotype-specific treatment responses**
686 We calculated the sensitivity and specificity for the three metrics, when 1) the
687 genotype-specific treatment responses to osimertinib only occur in large tumors, while smaller
688 tumors respond similarly to sg*Inert* tumors, 2) the genotype-specific treatment responses are
689 uniform across all tumor sizes such that all sg*TS* tumors have increased or reduced sensitivity to
690 osimertinib relative to sg*Inert* tumors (**Supplemental Figs. 6e, f**). Specifically, we used all ten
691 vehicle-treated mice at 11 weeks for simulation. We first applied a drug effect of K = 75% (75%
692 of cells are expected to be killed by osimertinib assuming no genotype-specific treatment
693 responses) to all tumors. Then we apply the preassigned genotype-specific treatment responses
694 to all tumors to generate the simulated distributed tumor sizes. For the first scenario of size-
695 dependent genotype-specific treatment response, the preassigned genotype-specific responses
696 only occur in tumors with over 10,000 cells, and they are assigned to be four-fold higher than
697 expected, i.e., these tumors do not respond at all to osimertinib considering that 75% of tumor
698 cells are expected to be killed without any genotype-specific treatment responses. For the
699 second scenario of uniform responses, all tumors with the sg*TS* are assigned to be 50% larger
700 than expected, i.e., reduced in size by 62.5% instead of 75% after treatment by osimertinib. The
701 same sample sizes of ten vehicle- and ten osimertinib-treated mice were generated from
702 bootstrapping mice and then bootstrapping tumors from each mouse prior to and after the
703 simulated effects of drug responses and genotype - specific responses, respectively. To
704 calculate the false discovery rate, we also simulated another scenario where no preassigned

705 genotype-specific responses exist and all tumors, regardless of genotypes, were reduced in size
706 uniformly by 75% by osimertinib. The therapeutic sensitivity was calculated as the probability of
707 re-identifying the preassigned genotype-specific treatment responses given the cutoff of *P*-
708 values, while specificity was calculated as the probability of falsely identifying genotype-specific
709 treatment responses without any input signal of genotype-specific treatment responses given
710 the cutoff of *P*-values. A total of 100 runs of simulations of the 11 tumor suppressor genes
711 (including Tp53; 1,100 cases) were performed for each scenario. We further plotted the
712 receiver operating characteristic[78] curves for the three metrics by varying the cutoff for the *P*-
713 values.
714
715 **Histology and immunohistochemistry**
716 The auxiliary lobe of the right lung was collected for each experimental mouse from the
717 mice transduced with the Lenti-sg*TS*^{Pool}*/Cre* pool whereas, both the auxiliary and left lobes were
718 collected for the validation experiments with individual sgRNAs (sg*Apc*, sg*Rbm10*, sg*Rbm10#2*
719 and sg*Neo2*). Right and auxiliary lobes were collected for the experiment with Lenti-
720 sg*Keap1/Cre* virus. Lung lobes were fixed in 4% paraformaldehyde overnight at room
721 temperature, placed in 70% ethanol, and paraffin-embedded and sectioned (Histology @ Yale).
722 Four micrometer sections were used for hematoxylin and eosin (H&E) staining and
723 immunohistochemistry. Tumor sizes were determined by measuring the longest diameter for
724 each tumor in H&E stained sections. Tumor size and tumor area were quantified using ImageJ.
725 The limited tissue collected for histological analysis reduced the number of tumors initiated
726 with Lenti-sg*Rbm10/Cre* that could be measured. *P*-values were calculated from the Mann-
727 Whitney U test. The following antibodies were used for immunohistochemistry: anti-mutant
728 EGFR^{L858R} (1:200, CST #3197), anti-SP-C (1:200, AB40876), anti-TTF-1/Nkx2-1 (1:200, AB76013),

729 anti-phospho-histone H3 (1:200, CST #9701), anti-Ki-67 (1:400, CST #9027), anti-mKate (1:2500,
730 Evrogen #AB233), anti-Cas9 (1:500, Novus Biologicals #7A9-3A3, NBP2-36440), anti-β-catenin
731 (1:500, CST #8814), anti-Rbm10 (1:200, AB224149), and anti-Keap1 (1:500, AB227828). Rbm10
732 expression in tumors was binned as High (over 75% of positive nuclei), Medium (between 25
733 and 75% of positive nuclei) or Low/negative (positive nuclear staining below 25%). Keap1 levels
734 in tumors were binned as High (over 75% of positive cells), Medium (between 25 and 75% of
735 positive cells) or Low/negative (positive staining below 25%). *P*-values were calculated using the
736 Chi-squared test.
737
738 **Analysis of human lung tumor data using GENIE data**
739 The AACR Project GENIE is a registry that contains CLIA-/ISO-certified genomic data
740 collected from the records of more than 9,000 patients who were treated at each of the
741 consortium's participating institutions[48]. Data from GENIE version 4.1-public were accessed
742 through the Synapse Platform. We generated a comprehensive list of all missense, nonsense,
743 and frameshift mutations for all screened genes across all participating centers in the GENIE
744 project, documenting these mutations at the gene and amino acid levels. Based on the sets of
745 genes included in the different screening panels that contribute to Project GENIE, we annotated
746 all lung adenocarcinoma within the database as being wild-type, mutated, or not screened for
747 each gene. From this complete catalog of mutations in each tumor, we determined the rates of
748 co-occurrence of known oncogenic *KRAS* mutations (G12X, G13X, Q61X) or *EGFR* mutations
749 (L858R, Exon 19 deletions, L861Q, G719X) with missense, nonsense, or frameshift mutations in
750 our set of ten tumor suppressor genes. Furthermore, we determined the frequency of co-
751 incident tumor suppressor gene mutations in tumors with oncogenic *KRAS* and inactivating
752 *TP53* mutations (*KRAS/TP53*) and in tumors with oncogenic *EGFR* and inactivating *TP53*

753 mutations (*EGFR/TP53*). A similar analysis was also performed on tumors with *ALK*-
754 rearrangements and *TP53* mutations using GENIE version 7.0 (**Supplemental Fig. 11**). A pipeline
755 for this analysis is publicly available at www.github.com/dgmaghini/GENIE, which allows users
756 to input OncoTree codes of interest, generate mutational profiles for the corresponding GENIE
757 tumors, and identify the co-occurrence of up to two background mutations (for example, *EGFR*
758 and *TP53*) with mutations in other genes of interest.
759

760 **Stanford cohort of *EGFR* mutant lung adenocarcinomas**

761 Patients with lung cancer who were evaluated at the Stanford Cancer Center and had
762 their tumors analyzed using the Stanford Solid Tumor Actionable Mutation Panel (STAMP)[6]
763 were included in the analysis. This retrospective study was conducted under a molecular
764 analysis protocol approved by the Stanford University Institutional Review Board. All STAMP
765 cases performed between 2015 and 2019 were included; during this time, there were two
766 different assays used, with one covering 198 genes (302 kb) and the other covering 130 genes
767 (232 kb). STAMP was done as the standard of care and thus at the discretion of the treating
768 physician and could have occurred at the time of diagnosis or at the time of progression.
769 From the available STAMP cases, patients were selected if they had stage IV non-small
770 cell lung cancer (NSCLC) and had a pathogenic *EGFR* and *p53* mutation. Patients were excluded
771 if they had incomplete data or were lost to follow up prior to analysis of the primary endpoint,
772 if they elected not to receive treatment or if they received adjuvant tyrosine kinase inhibitor
773 therapy for early-stage disease. Within this cohort, patients were further selected for the
774 presence of at least one of the tumor suppressor genes investigated in the preclinical setting
775 (*KEAP1, LKB1/STK11, SETD2, SMAD4, RB1, APC, ARIDIA* and/or *CDKN2A*). To ensure that there
776 was enough power to conduct an analysis, genes were analyzed individually if there were at

777 least 8 patients with tumors with a mutation of that gene who met inclusion criteria. Due to
778 small numbers, patients with tumors with *LKB1* (*N* = 1), *SETD2* (*N* = 0) and *SMAD4* (*N* = 1)
779 mutations were not analyzed separately. However, as the two patients with tumors harboring
780 *LKB1* and *SMAD4* mutations were also *EGFR/P53* mutant, they were included as part of the
781 control arm. Univariate analysis of time to treatment failure was completed on cases with stage
782 IV, *EGFR/P53* mutant NSCLC who were treated with a tyrosine kinase inhibitor [13] and had
783 mutations in either *KEAP1*-pathway component *(KEAP1, NFE2L2, CUL3), RB1, APC, ARIDIA* or
784 *CDKN2A.* Mutations that were significant on univariate analysis were identified and multivariate
785 analyses accounting for 1) co-founding variables and 2) co-mutations were run. Demographic
786 data including sex, age at diagnosis, smoking history, and ethnicity were extracted
787 (**Supplemental Tables 1, 2**). For each tumor suppressor, patients were matched 1:3 with a
788 wildtype cohort on the basis of sex, smoking history, ethnicity, age and treatment type. Time to
789 Treatment Failure [79] was determined by subtracting the date of discontinuation of TKI due to
790 progression, toxicity or death, from the date of initiation of TKI and reported in months.
791 Statistical analysis was performed using Prism 8 and R studio. The Kaplan-Meier method was
792 used to estimate TTF. Comparison of survival curves was made using the Log-rank test.
793 Significance was defined as $P < 0.05$. Hazard ratios (HR) were generated from multivariate
794 regression analysis performed in R and reported with a 95% confidence interval (CI).
795

796 **Yale cohort of *EGFR* mutant lung adenocarcinomas**

797 Patients with *EGFR*-mutant lung adenocarcinoma were consented and enrolled to a Yale
798 University IRB approved protocol allowing the collection and analysis of clinical data, archival
799 and fresh tissue, blood and the generation of patient-derived xenografts. Patients who received
800 targeted therapy (erlotinib, gefitinib, or afatinib) as first line therapy, either alone or in

801 combination with other therapies such as chemotherapy or cetuximab, were included
802 (**Supplemental Table 3**). For genomic studies, formalin-fixed paraffin embedded tissue was
803 macro-dissected to enrich for tumor material. All of the tumor samples (*N* = 29) analyzed had
804 matched normal tissue and cancer cell purity >20% as assessed by the LOH (Loss of
805 Heterozygosity) events from the whole exome sequencing data.

806 Whole Exome Sequencing

807 DNA was extracted from and analyzed as previously described[80]. Briefly, genomic DNA
808 was captured on the NimbleGen 2.1M human exome array and subjected to 74-bp paired-end
809 reads on the Illumina HiSeq2000 instrument. The mean coverage for normal was 109.1x and the
810 mean coverage for tumor was 189x with 92.78% and 95.56% for the bases covered at least 20
811 independent sequence reads, respectively. Sequence reads were mapped to the human
812 reference genome (GRCh37) using the Burrow-Wheeler Aligner-MEM (BWA-MEM) program.
813 Sequence reads outside the targeted sequences were discarded and the statistics on coverage
814 were collected from the remaining reads using in-house per scripts.

815 Somatic Mutation Calling

816 For all matched tumor-normal pairs, somatic point mutations and indels were called by
817 MuTect2 using Bayesian classifiers. For all somatic mutations called, we extracted base
818 coverage information in all samples and considered the mutations that were supported by at
819 least two independent sequence reads covering non-reference alleles and present in more than
820 5% of all sequencing reads. Identified variants were further filtered based on their presence in
821 repositories of common variations (1000 Genomes, NHLBI exome variant server and 2,577 non-
822 cancer exomes sequenced at Yale) and annotated using ANNOVAR program[81]. All somatic indels
823 were visually inspected to remove the false positive calls.

824 Somatic Copy Number Variation Analysis

825 Copy number analysis was performed as previously described[80]. Briefly, copy number
826 variants were identified from the whole exome sequencing data using EXCAVATOR software
827 that normalizes the non-uniform whole exome sequencing data taking GC-content, mappability,
828 and exon-size into account[82]. The Hidden Markov Model was utilized to classify each copy
829 number variant segment into five copy number states (homozygous deletion, heterozygous
830 deletion, normal copy number, homozygous copy gain or multiple copy gain). Tumor purity was
831 estimated from LOH using in-house per scripts.

832

833 **Data availability**

834 The datasets generated during and/or analyzed in the current study will be made available
835 in the NCBI Gene Expression Omnibus database (GSE146550) and dbGAP. GENIE genomic
836 data analysis is publicly available at www.github.com/dgmaghini/GENIE. All other data
837 supporting the findings are available upon request.

838

839 **Code availability**

840 The code is available at https://github.com/lichuan199010/Tuba-seq-analysis-and-
841 summary-statistics.

842

843 **References**
844

845 1 Hanahan, D. & Weinberg, R. A. Hallmarks of cancer: the next generation. *Cell* **144**, 646-
846 674, doi:10.1016/j.cell.2011.02.013 (2011).
847 2 Skoulidis, F. & Heymach, J. V. Co-occurring genomic alterations in non-small-cell lung
848 cancer biology and therapy. *Nat Rev Cancer* **19**, 495-509, doi:10.1038/s41568-019-
849 0179-8 (2019).
850 3 van de Haar, J. *et al.* Identifying Epistasis in Cancer Genomes: A Delicate Affair. *Cell*
851 **177**, 1375-1383, doi:10.1016/j.cell.2019.05.005 (2019).

852 4 Platt, R. J. *et al.* CRISPR-Cas9 knockin mice for genome editing and cancer modeling.
853 *Cell* **159**, 440-455, doi:10.1016/j.cell.2014.09.014 (2014).
854 5 Chen, S. *et al.* Genome-wide CRISPR screen in a mouse model of tumor growth and
855 metastasis. *Cell* **160**, 1246-1260, doi:10.1016/j.cell.2015.02.038 (2015).
856 6 Chuang, C. H. *et al.* Molecular definition of a metastatic lung cancer state reveals a
857 targetable CD109-Janus kinase-Stat axis. *Nat Med* **23**, 291-300, doi:10.1038/nm.4285
858 (2017).
859 7 Winters, I. P. *et al.* Multiplexed in vivo homology-directed repair and tumor barcoding
860 enables parallel quantification of Kras variant oncogenicity. *Nat Commun* **8**, 2053,
861 doi:10.1038/s41467-017-01519-y (2017).
862 8 Rogers, Z. N. *et al.* A quantitative and multiplexed approach to uncover the fitness
863 landscape of tumor suppression in vivo. *Nat Methods* **14**, 737-742,
864 doi:10.1038/nmeth.4297 (2017).
865 9 Rogers, Z. N. *et al.* Mapping the in vivo fitness landscape of lung adenocarcinoma
866 tumor suppression in mice. *Nat Genet* **50**, 483-486, doi:10.1038/s41588-018-0083-2
867 (2018).
868 10 Winters, I. P., Murray, C. W. & Winslow, M. M. Towards quantitative and multiplexed
869 in vivo functional cancer genomics. *Nat Rev Genet* **19**, 741-755, doi:10.1038/s41576-
870 018-0053-7 (2018).
871 11 Campbell, J. D. *et al.* Distinct patterns of somatic genome alterations in lung
872 adenocarcinomas and squamous cell carcinomas. *Nat Genet* **48**, 607-616,
873 doi:10.1038/ng.3564 (2016).
874 12 Cancer Genome Atlas Research, N. Comprehensive molecular profiling of lung
875 adenocarcinoma. *Nature* **511**, 543-550, doi:10.1038/nature13385 (2014).
876 13 Blakely, C. M. *et al.* Evolution and clinical impact of co-occurring genetic alterations in
877 advanced-stage EGFR-mutant lung cancers. *Nat Genet* **49**, 1693-1704,
878 doi:10.1038/ng.3990 (2017).
879 14 Politi, K. & Herbst, R. S. Lung cancer in the era of precision medicine. *Clin Cancer Res*
880 **21**, 2213-2220, doi:10.1158/1078-0432.CCR-14-2748 (2015).
881 15 Jordan, E. J. *et al.* Prospective Comprehensive Molecular Characterization of Lung
882 Adenocarcinomas for Efficient Patient Matching to Approved and Emerging Therapies.
883 *Cancer Discov* **7**, 596-609, doi:10.1158/2159-8290.CD-16-1337 (2017).
884 16 Jamal-Hanjani, M. *et al.* Tracking the Evolution of Non-Small-Cell Lung Cancer. *N Engl*
885 *J Med* **376**, 2109-2121, doi:10.1056/NEJMoa1616288 (2017).
886 17 Yu, H. A. *et al.* Concurrent Alterations in EGFR-Mutant Lung Cancers Associated with
887 Resistance to EGFR Kinase Inhibitors and Characterization of MTOR as a Mediator of
888 Resistance. *Clin Cancer Res* **24**, 3108-3118, doi:10.1158/1078-0432.CCR-17-2961
889 (2018).
890 18 Scheffler, M. *et al.* K-ras Mutation Subtypes in NSCLC and Associated Co-occuring
891 Mutations in Other Oncogenic Pathways. *J Thorac Oncol* **14**, 606-616,
892 doi:10.1016/j.jtho.2018.12.013 (2019).
893 19 Lynch, T. J. *et al.* Activating mutations in the epidermal growth factor receptor
894 underlying responsiveness of non-small-cell lung cancer to gefitinib. *N Engl J Med* **350**,
895 2129-2139, doi:10.1056/NEJMoa040938 (2004).
896 20 Paez, J. G. *et al.* EGFR mutations in lung cancer: correlation with clinical response to
897 gefitinib therapy. *Science* **304**, 1497-1500, doi:10.1126/science.1099314 (2004).

898 21 Pao, W. *et al.* EGF receptor gene mutations are common in lung cancers from "never
899 smokers" and are associated with sensitivity of tumors to gefitinib and erlotinib. *Proc*
900 *Natl Acad Sci U S A* **101**, 13306-13311, doi:10.1073/pnas.0405220101 (2004).
901 22 Soria, J. C. *et al.* Osimertinib in Untreated EGFR-Mutated Advanced Non-Small-Cell
902 Lung Cancer. *N Engl J Med* **378**, 113-125, doi:10.1056/NEJMoa1713137 (2018).
903 23 Offin, M. *et al.* Concurrent RB1 and TP53 Alterations Define a Subset of EGFR-Mutant
904 Lung Cancers at risk for Histologic Transformation and Inferior Clinical Outcomes. *J*
905 *Thorac Oncol*, doi:10.1016/j.jtho.2019.06.002 (2019).
906 24 DuPage, M. *et al.* Endogenous T cell responses to antigens expressed in lung
907 adenocarcinomas delay malignant tumor progression. *Cancer Cell* **19**, 72-85,
908 doi:10.1016/j.ccr.2010.11.011 (2011).
909 25 Caswell, D. R. *et al.* Obligate progression precedes lung adenocarcinoma
910 dissemination. *Cancer Discov* **4**, 781-789, doi:10.1158/2159-8290.CD-13-0862 (2014).
911 26 DuPage, M., Dooley, A. L. & Jacks, T. Conditional mouse lung cancer models using
912 adenoviral or lentiviral delivery of Cre recombinase. *Nat Protoc* **4**, 1064-1072,
913 doi:10.1038/nprot.2009.95 (2009).
914 27 Politi, K. *et al.* Lung adenocarcinomas induced in mice by mutant EGF receptors found
915 in human lung cancers respond to a tyrosine kinase inhibitor or to down-regulation of
916 the receptors. *Genes Dev* **20**, 1496-1510, doi:10.1101/gad.1417406 (2006).
917 28 Dow, L. E. *et al.* Conditional reverse tet-transactivator mouse strains for the efficient
918 induction of TRE-regulated transgenes in mice. *PLoS One* **9**, e95236,
919 doi:10.1371/journal.pone.0095236 (2014).
920 29 Jonkers, J. *et al.* Synergistic tumor suppressor activity of BRCA2 and p53 in a
921 conditional mouse model for breast cancer. *Nat Genet* **29**, 418-425,
922 doi:10.1038/ng747 (2001).
923 30 Chiou, S. H. *et al.* A conditional system to specifically link disruption of protein-coding
924 function with reporter expression in mice. *Cell Rep* **7**, 2078-2086,
925 doi:10.1016/j.celrep.2014.05.031 (2014).
926 31 Puglisi, F. *et al.* Prognostic value of thyroid transcription factor-1 in primary, resected,
927 non-small cell lung carcinoma. *Mod Pathol* **12**, 318-324 (1999).
928 32 Tan, D. *et al.* Thyroid transcription factor-1 expression prevalence and its clinical
929 implications in non-small cell lung cancer: a high-throughput tissue microarray and
930 immunohistochemistry study. *Hum Pathol* **34**, 597-604, doi:10.1016/s0046-
931 8177(03)00180-1 (2003).
932 33 Tanaka, H. *et al.* Lineage-specific dependency of lung adenocarcinomas on the lung
933 development regulator TTF-1. *Cancer Res* **67**, 6007-6011, doi:10.1158/0008-
934 5472.CAN-06-4774 (2007).
935 34 Nakayama, S. *et al.* beta-catenin contributes to lung tumor development induced by
936 EGFR mutations. *Cancer Res* **74**, 5891-5902, doi:10.1158/0008-5472.CAN-14-0184
937 (2014).
938 35 Zehir, A. *et al.* Mutational landscape of metastatic cancer revealed from prospective
939 clinical sequencing of 10,000 patients. *Nat Med* **23**, 703-713, doi:10.1038/nm.4333
940 (2017).
941 36 Bechara, E. G., Sebestyen, E., Bernardis, I., Eyras, E. & Valcarcel, J. RBM5, 6, and 10
942 differentially regulate NUMB alternative splicing to control cancer cell proliferation.
943 *Mol Cell* **52**, 720-733, doi:10.1016/j.molcel.2013.11.010 (2013).

944 37 Hernandez, J. *et al.* Tumor suppressor properties of the splicing regulatory factor
945 RBM10. *RNA Biol* **13**, 466-472, doi:10.1080/15476286.2016.1144004 (2016).
946 38 Zhao, J. *et al.* Functional analysis reveals that RBM10 mutations contribute to lung
947 adenocarcinoma pathogenesis by deregulating splicing. *Sci Rep* **7**, 40488,
948 doi:10.1038/srep40488 (2017).
949 39 Walter, D. M. *et al.* Systematic In Vivo Inactivation of Chromatin-Regulating Enzymes
950 Identifies Setd2 as a Potent Tumor Suppressor in Lung Adenocarcinoma. *Cancer Res*
951 **77**, 1719-1729, doi:10.1158/0008-5472.CAN-16-2159 (2017).
952 40 Ji, H. *et al.* LKB1 modulates lung cancer differentiation and metastasis. *Nature* **448**,
953 807-810, doi:10.1038/nature06030 (2007).
954 41 Sanchez-Rivera, F. J. *et al.* Rapid modelling of cooperating genetic events in cancer
955 through somatic genome editing. *Nature* **516**, 428-431, doi:10.1038/nature13906
956 (2014).
957 42 Jackson, E. L. *et al.* Analysis of lung tumor initiation and progression using conditional
958 expression of oncogenic K-ras. *Genes Dev* **15**, 3243-3248, doi:10.1101/gad.943001
959 (2001).
960 43 Schuster, K. *et al.* Nullifying the CDKN2AB locus promotes mutant K-ras lung
961 tumorigenesis. *Mol Cancer Res* **12**, 912-923, doi:10.1158/1541-7786.MCR-13-0620-T
962 (2014).
963 44 Schmitt, A. *et al.* ATM Deficiency Is Associated with Sensitivity to PARP1- and ATR
964 Inhibitors in Lung Adenocarcinoma. *Cancer Res* **77**, 3040-3056, doi:10.1158/0008-
965 5472.CAN-16-3398 (2017).
966 45 Efeyan, A. *et al.* Limited role of murine ATM in oncogene-induced senescence and p53-
967 dependent tumor suppression. *PLoS One* **4**, e5475, doi:10.1371/journal.pone.0005475
968 (2009).
969 46 Ho, V. M., Schaffer, B. E., Karnezis, A. N., Park, K. S. & Sage, J. The retinoblastoma gene
970 Rb and its family member p130 suppress lung adenocarcinoma induced by oncogenic
971 K-Ras. *Oncogene* **28**, 1393-1399, doi:10.1038/onc.2008.491 (2009).
972 47 Walter, D. M. *et al.* RB constrains lineage fidelity and multiple stages of tumour
973 progression and metastasis. *Nature* **569**, 423-427, doi:10.1038/s41586-019-1172-9
974 (2019).
975 48 Consortium, A. P. G. AACR Project GENIE: Powering Precision Medicine through an
976 International Consortium. *Cancer Discov* **7**, 818-831, doi:10.1158/2159-8290.CD-17-
977 0151 (2017).
978 49 Skoulidis, F. *et al.* Co-occurring genomic alterations define major subsets of KRAS-
979 mutant lung adenocarcinoma with distinct biology, immune profiles, and therapeutic
980 vulnerabilities. *Cancer Discov* **5**, 860-877, doi:10.1158/2159-8290.CD-14-1236 (2015).
981 50 Arbour, K. C. *et al.* Effects of Co-occurring Genomic Alterations on Outcomes in
982 Patients with KRAS-Mutant Non-Small Cell Lung Cancer. *Clin Cancer Res* **24**, 334-340,
983 doi:10.1158/1078-0432.CCR-17-1841 (2018).
984 51 Gealy, R., Zhang, L., Siegfried, J. M., Luketich, J. D. & Keohavong, P. Comparison of
985 mutations in the p53 and K-ras genes in lung carcinomas from smoking and
986 nonsmoking women. *Cancer Epidemiol Biomarkers Prev* **8**, 297-302 (1999).
987 52 Pirazzoli, V. *et al.* Afatinib plus Cetuximab Delays Resistance Compared to Single-Agent
988 Erlotinib or Afatinib in Mouse Models of TKI-Naive EGFR L858R-Induced Lung
989 Adenocarcinoma. *Clin Cancer Res* **22**, 426-435, doi:10.1158/1078-0432.CCR-15-0620
990 (2016).

991 53 Pirazzoli, V. *et al.* Acquired resistance of EGFR-mutant lung adenocarcinomas to
992 afatinib plus cetuximab is associated with activation of mTORC1. *Cell Rep* **7**, 999-1008,
993 doi:10.1016/j.celrep.2014.04.014 (2014).
994 54 Starrett, J. H. G., A.; Cuomo, M.E.; Poels, K.; van Alderwerelt van Rosenburgh I.;
995 Nagelberg, A.; Farnsworth, D.; Price, K.S.; Khan, H.; Asthtekar, K.D.; Gaefele, M.; Ayeni,
996 D.; Stewart, T.F.; Kuhlmann, A.; Keack, S.; Unni, A.M.; Homer, R.; Lockwood, W.W.;
997 Michor, F.; Goldberg, S.B.; Lemmon, M.A.; Smith, P.D.; Cross, D.A.; Politi, K. Drug
998 sensitivity and allele-specificity of first-line osimertinib resistance *EGFR* mutations.
999 *Under Revision* (2020).
1000 55 Ramalingam, S. S. *et al.* Osimertinib As First-Line Treatment of EGFR Mutation-Positive
1001 Advanced Non-Small-Cell Lung Cancer. *J Clin Oncol* **36**, 841-849,
1002 doi:10.1200/JCO.2017.74.7576 (2018).
1003 56 Ramalingam, S. S. *et al.* Overall Survival with Osimertinib in Untreated, EGFR-Mutated
1004 Advanced NSCLC. *N Engl J Med*, doi:10.1056/NEJMoa1913662 (2019).
1005 57 Li, C. L., W.; Rizvi, H.; Cai, H; McFarland, C.D.; Rogers, Z.N.; Yousefi, M.; Winters, I.P.;
1006 Rudin, C.M.; Petro, D.A.; Winslow, M.M. Quantitative *in vivo* analyses reveal a complex
1007 pharmacogenomic landscape in lung adenocarcinoma. *BioRxiv [**Preprint**] January 29,*
1008 *2020. Available from: https://doi.org/10.1101/2020.01.28.923912* (2020).
1009 58 Hellyer, J. A. *et al.* Impact of KEAP1/NFE2L2/CUL3 mutations on duration of response
1010 to EGFR tyrosine kinase inhibitors in EGFR mutated non-small cell lung cancer. *Lung*
1011 *Cancer* **134**, 42-45, doi:10.1016/j.lungcan.2019.05.002 (2019).
1012 59 Cleasby, A. *et al.* Structure of the BTB domain of Keap1 and its interaction with the
1013 triterpenoid antagonist CDDO. *PLoS One* **9**, e98896,
1014 doi:10.1371/journal.pone.0098896 (2014).
1015 60 Gainor, J. F. *et al.* ALK rearrangements are mutually exclusive with mutations in EGFR
1016 or KRAS: an analysis of 1,683 patients with non-small cell lung cancer. *Clin Cancer Res*
1017 **19**, 4273-4281, doi:10.1158/1078-0432.CCR-13-0318 (2013).
1018 61 Unni, A. M., Lockwood, W. W., Zejnullahu, K., Lee-Lin, S. Q. & Varmus, H. Evidence that
1019 synthetic lethality underlies the mutual exclusivity of oncogenic KRAS and EGFR
1020 mutations in lung adenocarcinoma. *Elife* **4**, e06907, doi:10.7554/eLife.06907 (2015).
1021 62 Kersten, K., de Visser, K. E., van Miltenburg, M. H. & Jonkers, J. Genetically engineered
1022 mouse models in oncology research and cancer medicine. *EMBO Mol Med* **9**, 137-153,
1023 doi:10.15252/emmm.201606857 (2017).
1024 63 Yamadori, T. *et al.* Molecular mechanisms for the regulation of Nrf2-mediated cell
1025 proliferation in non-small-cell lung cancers. *Oncogene* **31**, 4768-4777,
1026 doi:10.1038/onc.2011.628 (2012).
1027 64 Krall, E. B. *et al.* KEAP1 loss modulates sensitivity to kinase targeted therapy in lung
1028 cancer. *Elife* **6**, doi:10.7554/eLife.18970 (2017).
1029 65 Park, S. H. *et al.* Resistance to gefitinib and cross-resistance to irreversible EGFR-TKIs
1030 mediated by disruption of the Keap1-Nrf2 pathway in human lung cancer cells. *FASEB*
1031 *J*, fj201800011R, doi:10.1096/fj.201800011R (2018).
1032 66 DeNicola, G. M. *et al.* NRF2 regulates serine biosynthesis in non-small cell lung cancer.
1033 *Nat Genet* **47**, 1475-1481, doi:10.1038/ng.3421 (2015).
1034 67 Romero, R. *et al.* Keap1 loss promotes Kras-driven lung cancer and results in
1035 dependence on glutaminolysis. *Nat Med* **23**, 1362-1368, doi:10.1038/nm.4407 (2017).
1036 68 Galan-Cobo, A. *et al.* LKB1 and KEAP1/NRF2 Pathways Cooperatively Promote
1037 Metabolic Reprogramming with Enhanced Glutamine Dependence in KRAS-Mutant

1038 Lung Adenocarcinoma. *Cancer Res* **79**, 3251-3267, doi:10.1158/0008-5472.CAN-18-
1039 3527 (2019).
1040 69 Wang, J. *et al.* Nestin regulates cellular redox homeostasis in lung cancer through the
1041 Keap1-Nrf2 feedback loop. *Nat Commun* **10**, 5043, doi:10.1038/s41467-019-12925-9
1042 (2019).
1043 70 Jain, A. *et al.* p62/SQSTM1 is a target gene for transcription factor NRF2 and creates a
1044 positive feedback loop by inducing antioxidant response element-driven gene
1045 transcription. *J Biol Chem* **285**, 22576-22591, doi:10.1074/jbc.M110.118976 (2010).
1046 71 Wang, Q. *et al.* CDK20 interacts with KEAP1 to activate NRF2 and promotes
1047 radiochemoresistance in lung cancer cells. *Oncogene* **36**, 5321-5330,
1048 doi:10.1038/onc.2017.161 (2017).
1049 72 Marcar, L. *et al.* Acquired Resistance of EGFR-Mutated Lung Cancer to Tyrosine Kinase
1050 Inhibitor Treatment Promotes PARP Inhibitor Sensitivity. *Cell Rep* **27**, 3422-3432
1051 e3424, doi:10.1016/j.celrep.2019.05.058 (2019).
1052 73 Madisen, L. *et al.* A robust and high-throughput Cre reporting and characterization
1053 system for the whole mouse brain. *Nat Neurosci* **13**, 133-140, doi:10.1038/nn.2467
1054 (2010).
1055 74 Nakada, D., Saunders, T. L. & Morrison, S. J. Lkb1 regulates cell cycle and energy
1056 metabolism in haematopoietic stem cells. *Nature* **468**, 653-658,
1057 doi:10.1038/nature09571 (2010).
1058 75 Hill, A. J. *et al.* On the design of CRISPR-based single-cell molecular screens. *Nat*
1059 *Methods* **15**, 271-274, doi:10.1038/nmeth.4604 (2018).
1060 76 Annunziato, S. *et al.* Modeling invasive lobular breast carcinoma by CRISPR/Cas9-
1061 mediated somatic genome editing of the mammary gland. *Genes Dev* **30**, 1470-1480,
1062 doi:10.1101/gad.279190.116 (2016).
1063 77 Papademetris, X. *et al.* BioImage Suite: An integrated medical image analysis suite: An
1064 update. *Insight J* **2006**, 209 (2006).
1065 78 Skoulidis, F. *et al.* STK11/LKB1 Mutations and PD-1 Inhibitor Resistance in KRAS-
1066 Mutant Lung Adenocarcinoma. *Cancer Discov* **8**, 822-835, doi:10.1158/2159-8290.CD-
1067 18-0099 (2018).
1068 79 Reck, M. *et al.* Pembrolizumab versus Chemotherapy for PD-L1-Positive Non-Small-
1069 Cell Lung Cancer. *N Engl J Med* **375**, 1823-1833, doi:10.1056/NEJMoa1606774 (2016).
1070 80 Choi, M. *et al.* Genetic diagnosis by whole exome capture and massively parallel DNA
1071 sequencing. *Proc Natl Acad Sci U S A* **106**, 19096-19101,
1072 doi:10.1073/pnas.0910672106 (2009).
1073 81 Wang, K., Li, M. & Hakonarson, H. ANNOVAR: functional annotation of genetic variants
1074 from high-throughput sequencing data. *Nucleic Acids Res* **38**, e164,
1075 doi:10.1093/nar/gkq603 (2010).
1076 82 Xu, D., Olman, V., Wang, L. & Xu, Y. EXCAVATOR: a computer program for efficiently
1077 mining gene expression data. *Nucleic Acids Res* **31**, 5582-5589,
1078 doi:10.1093/nar/gkg783 (2003).
1079

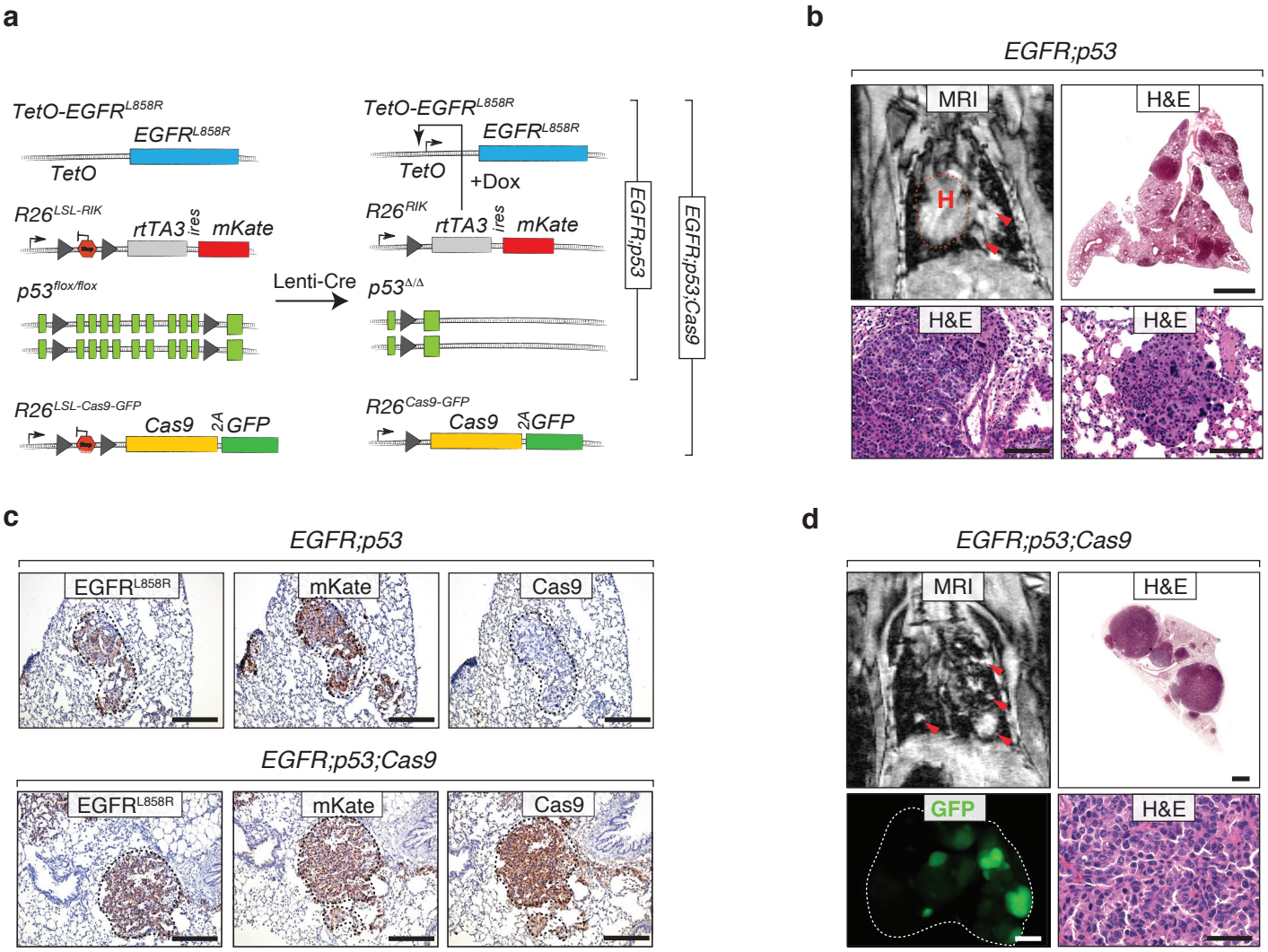

Fig. 1 | Lentiviral Cre-mediated lung tumor initiation in *EGFR;p53* and *EGFR;p53;Cas9* mice. a, Schematic of the *TetO-EGFR*^{L858R}, *R26*$^{LSL\text{-}RIK}$, and *p53*^{flox} alleles in *EGFR;p53* mice, prior to and following Cre-mediated recombination. Conditional expression of oncogenic EGFR^{L858R} is under the control of a tetracycline response element (*TetO*), which is induced by rtTA in the presence of doxycycline (Dox). Lentiviral-Cre inactivates *Trp53* and enables the expression of the reverse tetracycline-regulated transactivator (*rtTA3*) and mKate (from the *R26*$^{LSL\text{-}RIK}$ allele). Cre also allows expression of Cas9 and GFP (from the *R26*$^{LSL\text{-}Cas9\text{-}GFP}$ allele) in *EGFR;p53;Cas9* mice. **b**, MRI showing tumor development 11 weeks after tumor initiation in *EGFR;p53* mice (top left panel) with 2×10^6 ifu Lenti-Cre. The dashed red line surrounds the heart (H) and red arrows indicate areas of tumor. Hematoxylin and eosin (H&E) staining shows lung adenocarcinoma development. Scale bars = 1.2 mm and 100 µm in the top and bottom panels, respectively. Images are from a representative mouse ($N = 5$). **c**, Immunostaining for EGFR^{L858R}, mKate and Cas9 in tumors in *EGFR;p53* and *EGFR;p53;Cas9* mice. The dashed lines indicate areas of tumor. Scale bars = 200 µm. **d**, MRI and H&E showing tumor development 16 weeks after tumor initiation in *EGFR;p53;Cas9* mice with 1×10^5 ifu Lenti-Cre.Tumors are positive for GFP in *EGFR;p53;Cas9* mice and lungs are indicated by the white dashed line. H&E image scale bars = 1.2 mm and 100 µm in top and bottom right panels, respectively. GFP image scale bar = 2.5 mm.

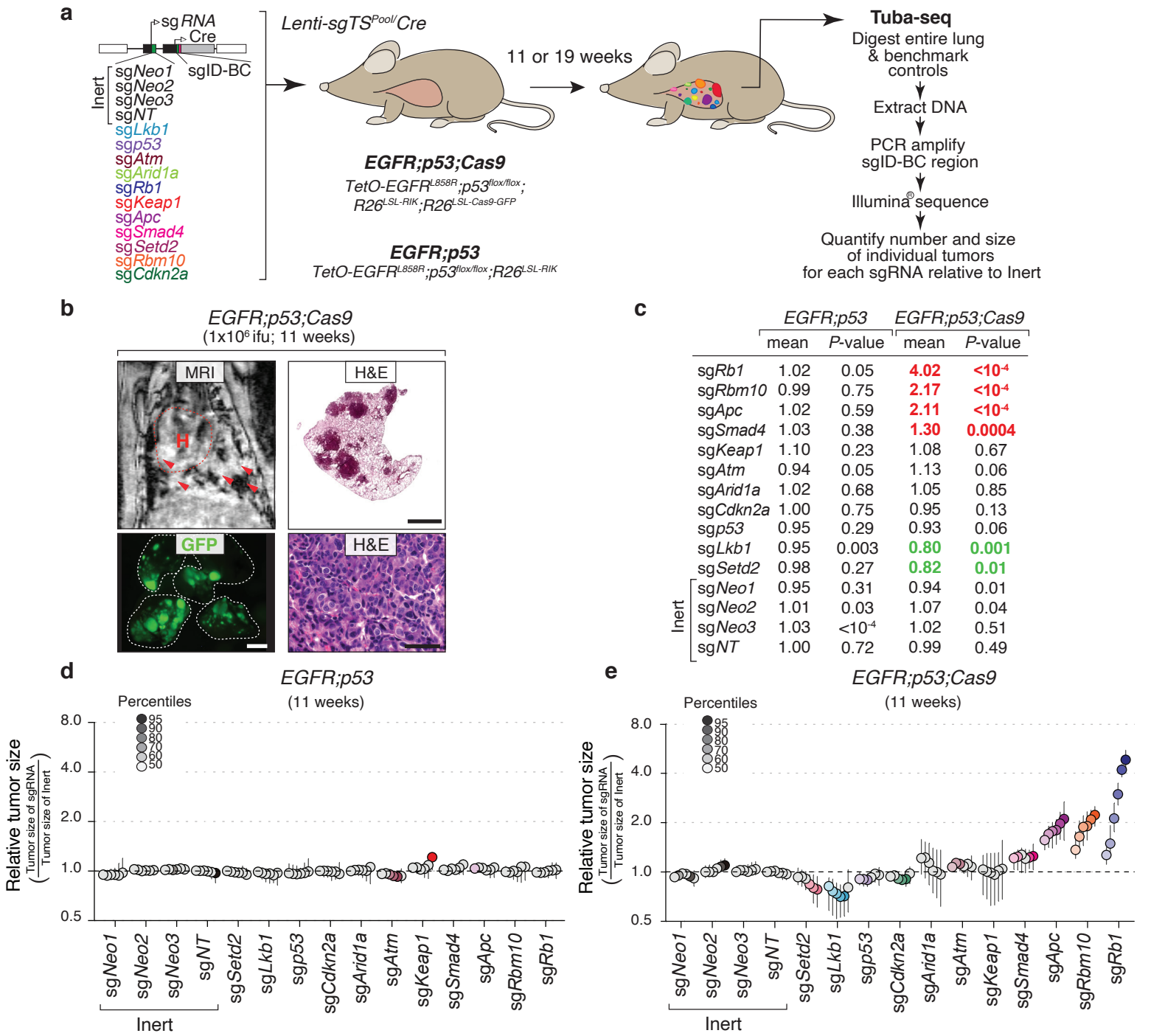

		EGFR;p53		EGFR;p53;Cas9	
		mean	*P*-value	mean	*P*-value
	sg*Rb1*	1.02	0.05	**4.02**	**<10⁻⁴**
	sg*Rbm10*	0.99	0.75	**2.17**	**<10⁻⁴**
	sg*Apc*	1.02	0.59	**2.11**	**<10⁻⁴**
	sg*Smad4*	1.03	0.38	**1.30**	**0.0004**
	sg*Keap1*	1.10	0.23	1.08	0.67
	sg*Atm*	0.94	0.05	1.13	0.06
	sg*Arid1a*	1.02	0.68	1.05	0.85
	sg*Cdkn2a*	1.00	0.75	0.95	0.13
	sg*p53*	0.95	0.29	0.93	0.06
	sg*Lkb1*	0.95	0.003	**0.80**	**0.001**
	sg*Setd2*	0.98	0.27	**0.82**	**0.01**
Inert	sg*Neo1*	0.95	0.31	0.94	0.01
Inert	sg*Neo2*	1.01	0.03	1.07	0.04
Inert	sg*Neo3*	1.03	<10⁻⁴	1.02	0.51
Inert	sg*NT*	1.00	0.72	0.99	0.49

Fig. 2 | Multiplexed somatic CRISPR–Cas9-mediated genome editing uncovers tumor suppressor gene effects on *EGFR*-driven lung tumors. a, Experimental strategy. Tumors were allowed to develop for either 11 weeks in *EGFR;p53;Cas9* and *EGFR;p53* mice or 19 weeks in *EGFR;p53;Cas9* mice after intra-tracheal administration of Lenti-sg*TS*^{Pool}*/Cre*. Whole lungs were collected for tumor barcode deep sequencing (Tuba-seq) and histology. The number of neoplastic cells in each tumor (tumor size) was calculated from barcode sequencing of bulk tumor-bearing lungs. Barcode read number was normalized to benchmark control cells that have known barcodes and were added at a known number to each sample (Methods). **b**, MRI, H&E, and GFP images showing tumor development in *EGFR;p53;-Cas9* mice 11 weeks after tumor initiation with 1x10^6 ifu of Lenti-sg*TS*^{Pool}*/Cre*. H&E image scale bars = 1.2 mm and 100 µm in top and bottom right panels, respectively. Lungs are indicated by the white dashed lines. GFP image scale bar = 2.5 mm. Images are from a representative mouse (N = 10). **c**, Relative log-normal (LN) mean size of tumors with each sgRNA in *EGFR;p53* (N = 5) and *EGFR;p53;-Cas9* mice (N = 10) 11 weeks after tumor initiation (normalized to the tumors with inert sgRNAs). *P*-values were calculated from bootstrap-ping. *P*-values < 0.05 and their corresponding means are highlighted in *EGFR;p53;Cas9* mice for sgRNAs that positively (red) and negatively (green) affect tumor growth when the effects are equal to or differ >10% compared to the size of tumors with inert sgRNAs. **d**, Relative size of tumors at the indicated percentiles of each genotype in *EGFR;p53* mice 11 weeks after tumor initiation with the Lenti-sg*TS*^{Pool}*/Cre*. These mice lack the *R26*$^{LSL\text{-}Cas9\text{-}GFP}$ allele; therefore, all sgRNAs are functionally inert. 95% confidence intervals are shown. Percentiles calculated from bootstrapping that are significantly different from the tumors with inert sgRNAs are in color. **e**, Relative size of tumors of each genotype in *EGFR;p53;Cas9* mice 11 weeks after tumor initiation with the Lenti-sg*TS*^{Pool}*/Cre*. The relative size of tumors at the indicated percentiles were calculated from the tumor size distribution of all tumors from ten mice. 95% confidence intervals are shown. Percentiles were calculated from bootstrapping and are in color if significantly different from the tumors with inert sgRNAs.

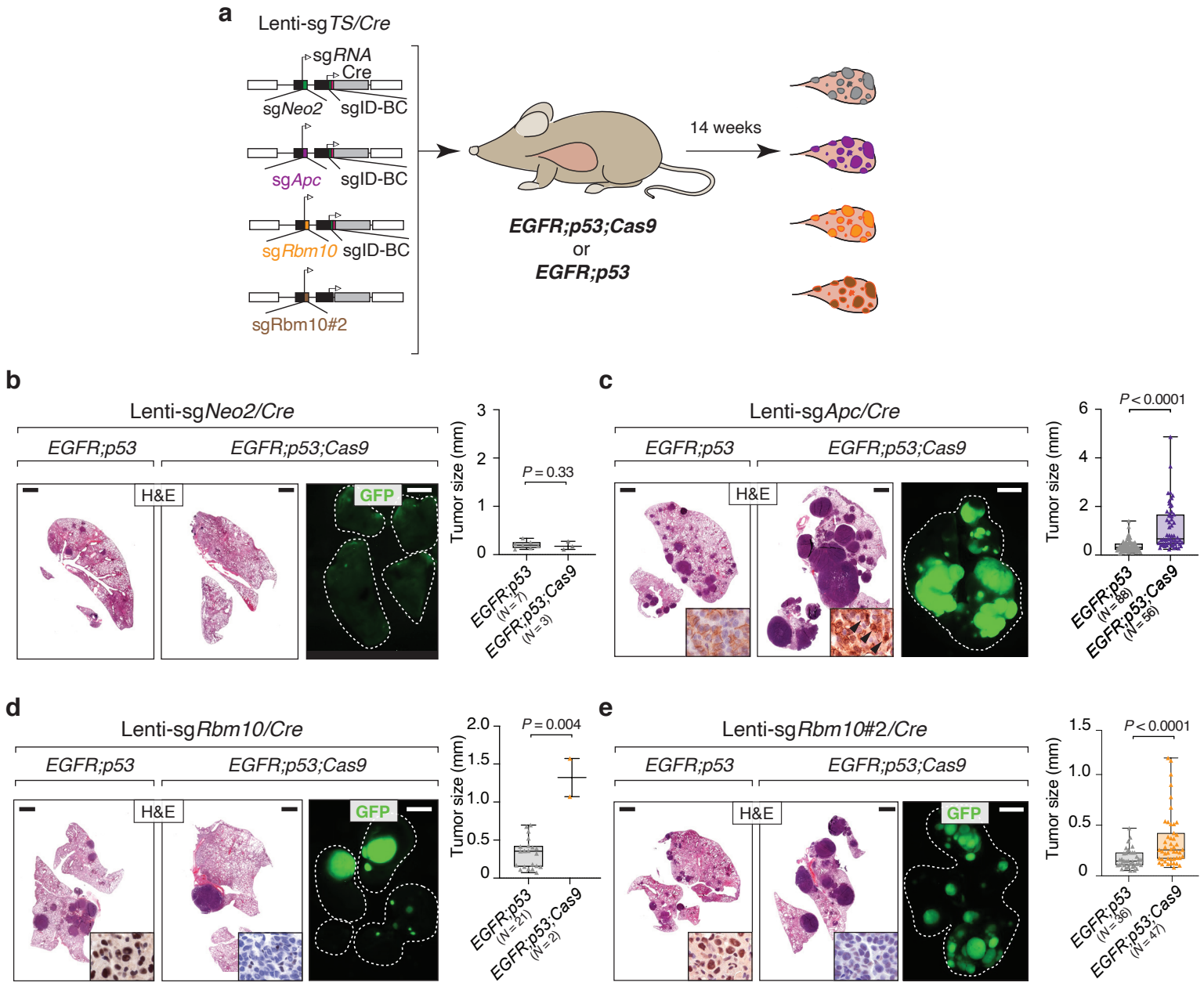

Fig. 3 | *Apc* and *Rbm10* inactivation enhances the growth of oncogenic *EGFR*-driven lung tumors *in vivo*. a, Experimental strategy for tumor suppressor gene validation. Tumors were initiated in *EGFR;p53* and *EGFR;p53;Cas9* mice with Lenti-sg*TS/Cre* vectors carrying sg*Apc*, sg*Rbm10*, sg*Rbm10#2*, or sg*Neo2* as a control (*EGFR;p53* $N = 3$ mice/group, *EGFR;p53;Cas9* $N = 5$ mice/group, 1×10^5 ifu/mouse). **b-e**, H&E and GFP images show that *Apc* (**c**) and *Rbm10* (**d, e**) inactivation enhances tumor growth compared to the controls (**b**). The histology of the left and auxiliary lobes was analyzed. Lungs are indicated by the white dashed lines. Scale bars = 1.2 mm and 2.5 mm for histology and GFP images, respectively. Tumor size was calculated by measuring the longest diameter of each tumor. The number of tumors studied are reported on the X-axis. *P*-values were calculated using a one-tailed Mann-Whitney U test. Horizontal lines show the median and whiskers indicate the minimum and the maximum of the data set. The box represents values in the first and the third quartile. The panels on the bottom right of the H&E images show nuclear accumulation of β-catenin (**c**) and absence of Rbm10 protein expression (**d, e**) reflective of *Apc* and *Rbm10* inactivation in tumors in *EGFR;p53;Cas9* mice, respectively.

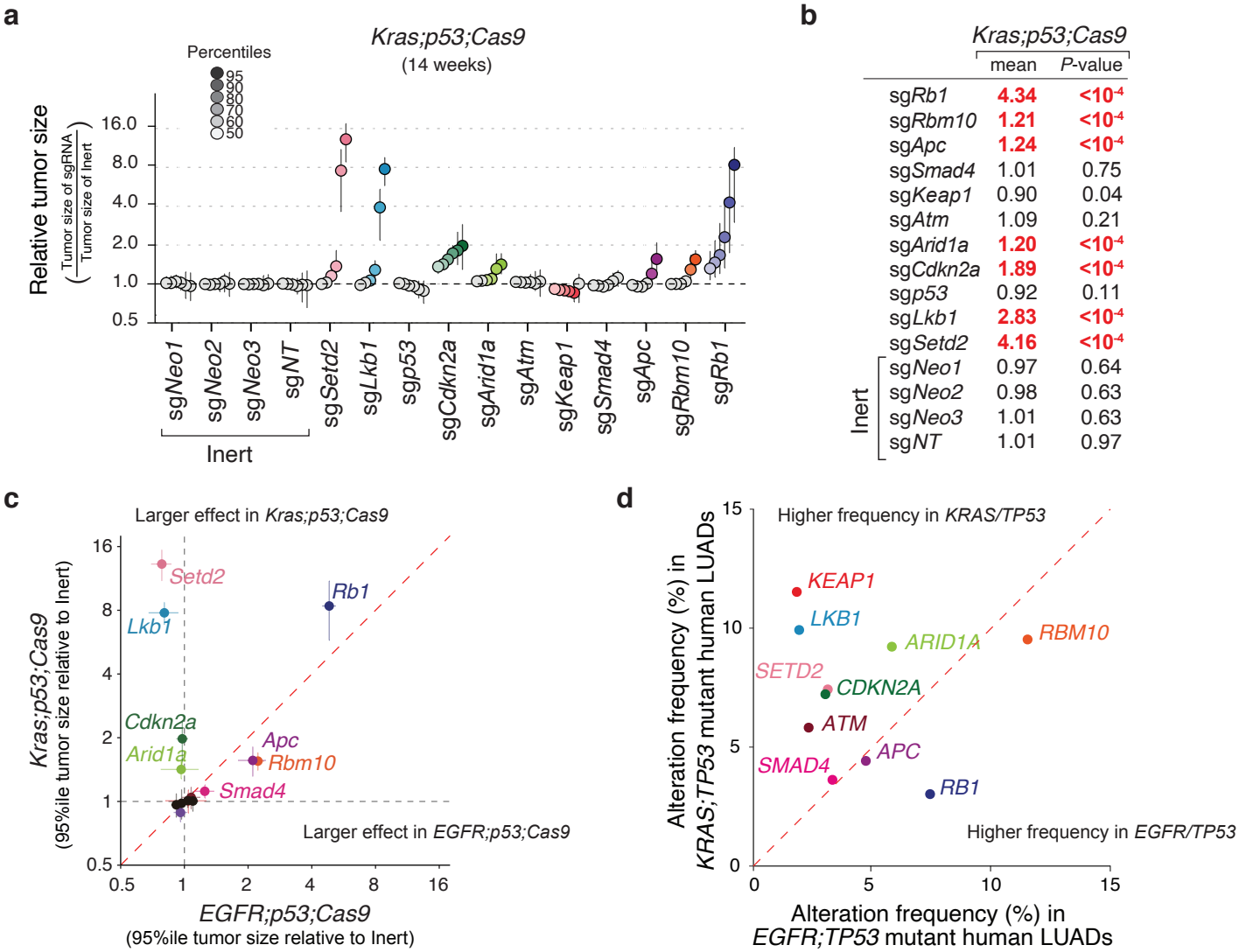

Fig. 4 | Dramatic differences in the effects of tumor suppressor genes in oncogenic *EGFR*- versus *Kras*-driven lung cancer. a, Relative size of tumors of each genotype in *Kras*^{G12D};*p53*$^{flox/flox}$;*R26*$^{LSL\text{-}Tomato}$;*H11*$^{LSL\text{-}Cas9}$ (*Kras;p53;Cas9*) mice 14 weeks after tumor initiation with Lenti-sg*TS*^{Pool}/*Cre* relative to tumors with inert sgRNAs. The relative size of tumors at the indicated percentiles was calculated from the tumor size distribution of all tumors from six mice. 95% confidence intervals are shown. *P*-values were calculated from bootstrapping. Percentiles that are significantly different from the tumors with inert sgRNAs are in color. **b**, LN mean for tumors with each sgRNA in *Kras;p53;Cas9* mice 14 weeks after tumor initiation (normalized to the inert tumors). *P*-values were calculated by bootstrapping and significant values are highlighted in red when $P < 0.05$ and the effects are >10% compared to the size of tumors with inert sgRNAs. **c**, The relative effect of inactivating each tumor suppressor gene on tumor sizes (comparison to tumors with inert sgRNAs) at the indicated percentile in the *EGFR;p53;Cas9* ($N = 10$) and *Kras;p53;Cas9* ($N = 6$) models. *Lkb1* and *Setd2* inactivation greatly increased tumor size only in the *Kras;p53;Cas9* model. Error bars indicate the standard deviation. **d**, The frequency of tumor suppressor gene alterations that co-occur with *EGFR* or *KRAS* and *TP53* mutations in human lung adenocarcinomas (LUADs, data from AACR Project GENIE). **e**, *LKB1* and *SETD2* alterations co-occur significantly more frequently in *KRAS*^{onc};*TP53*^{mut} than in *EGFR*^{onc};*TP53*^{mut} human lung adenocarcinomas. The frequency of *RBM10* and *APC* alterations were not significantly different between in *KRAS*^{onc};*TP53*^{mut} and *EGFR*^{onc};*TP53*^{mut} tumors. The odds ratios represent the strength of the observed frequencies of tumor suppressor gene alterations that co-occur in *KRAS*^{onc};*TP53*^{mut} cases compared to *EGFR*^{onc};*TP53*^{mut} cases. *P*-values were calculated using a Fisher's exact test.

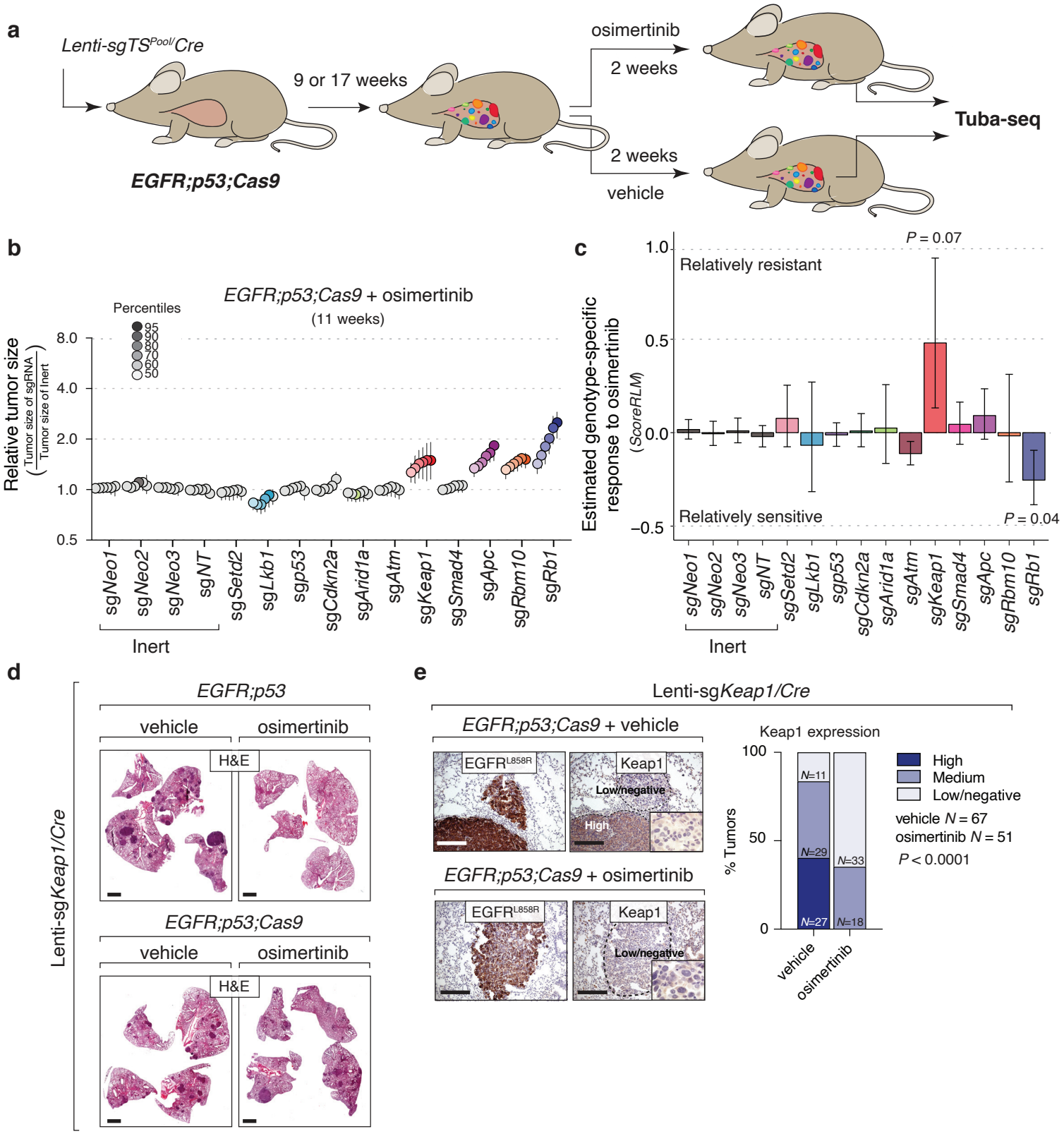

Fig. 5 | Identification of genotype-specific responses to osimertinib treatment. a, Experimental strategy. Tumors were initiated with Lenti-sg*TS^Pool/Cre* in *EGFR;p53;Cas9* mice for nine or 17 weeks and were treated for two weeks with either vehicle or osimertinib (25 mg/kg, 5 days/week). **b**, Relative size of the tumors at the indicated percentiles for each genotype in *EGFR;p53;Cas9* mice after treatment with osimertinib. 95% confidence intervals are shown. *P*-values were calculated from bootstrapping. Percentiles that are significantly different from the tumors with inert sgRNAs are in color. **c**, Estimate of the genotype-specific treatment response (*ScoreRLM*) calculated by comparing the LN mean of tumors treated with osimertinib to the LN mean of vehicle-treated tumors in *EGFR; p53;Cas9* mice 11 weeks after tumor initiation (Methods). Error bars indicate the standard deviation. *P*-values were calculated from bootstrapping. **d**, H&E staining of tumor bearing-lungs in *EGFR;p53* and *EGFR;p53;Cas9* mice with Lenti-sg*Keap1/Cre* initiated tumors ($N = 8$ mice/group). Scale bars = 1.2 mm. **e**, Immunostaining of Lenti-sg*Keap1/Cre* initiated tumors in *EGFR;p53;Cas9* mice for EGFR^L858R and Keap1 after vehicle or osimertinib treatment ($N = 4$ mice/treated-group). Tumors are still detectable after two weeks of treatment with osimertinib and mostly express medium or low/negative levels of Keap1 compared to tumors treated with vehicle in *EGFR;p53;Cas9* mice (bar graph). The dashed lines indicate areas of tumors and the level of Keap1 is indicated with a label (high or low/negative). Scale bars = 200 µm. *P*-values were calculated using a Chi-squared test.

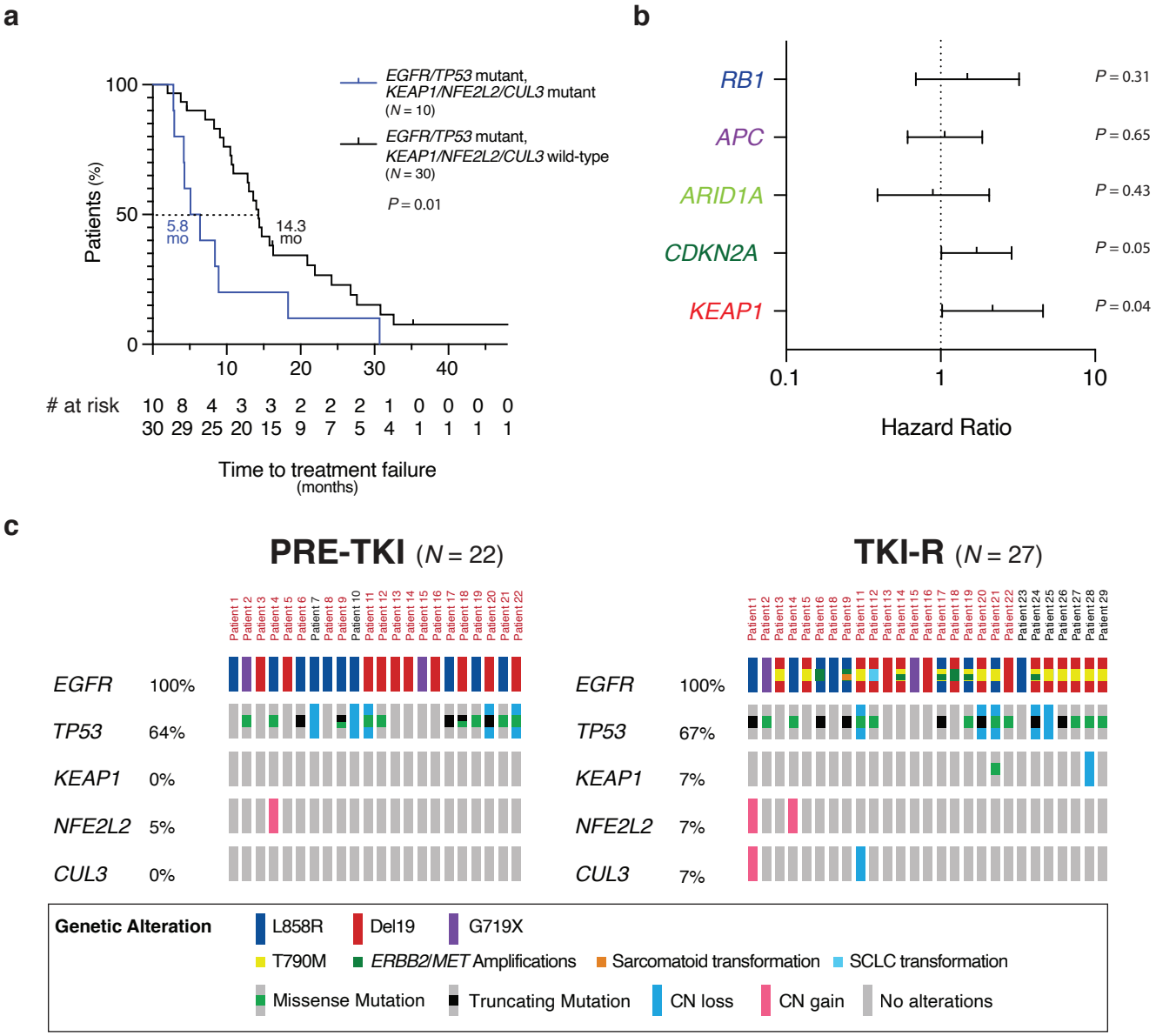

Fig. 6 | *KEAP1* inactivation correlates with reduced therapeutic response to TKIs in human *EGFR*-driven lung adenocarcinomas. a, Kaplan-Meier curve showing time to TKI treatment failure for patients with *EGFR/TP53* lung adenocarcinomas that do or not have mutations in the *KEAP1/NFE2L2/CUL3* axis. Time to treatment failure is the time from the initiation of TKI treatment to the date of discontinuation of TKI due to progression, toxicity or death. The *P*-value was calcuated using the Log rank test. **b**, Forest plot of the time on treatment hazard ratios for tumors with *KEAP1*, *RB1*, *APC*, *ARIDA* or *CDKN2A* alterations in *EGFR/TP53* mutant lung adenocarcinomas. Hazard ratios were calculated from multivariate regression analysis, 95% confidence intervals are shown. **c**, *KEAP1, NFE2L2*, and *CUL3* alteration frequency in oncogenic *EGFR* and *TP53* mutant lung tumors in the Yale Lung Rebiopsy Program dataset (Methods). OncoPrint of oncogenic *EGFR* samples prior to first-line TKI (erlotinib, gefitinib, afatinib) treatment (PRE-TKI, left panel) (*N* = 22), and at acquired resistance to TKIs (TKI-R, right panel) (*N* = 27). In each row, the percentage and the type of alterations in each gene are indicated for each patient. For the TKI-R samples, known resistance mechanisms such as acquisition of T790M in *EGFR*, are reported. Cases with paired PRE-TKI and TKI-R samples are indicated by the patient number highlighted in red.